SCALING RELATIONS OF CLUSTERS OF GALAXIES

A thesis submitted to the University of Manchester
for the degree of Master of Science
in the Faculty of Engineering and Physical Sciences

October 2013

By

David Boulderstone

School of Physics and Astronomy

Contents

List of Tables

List of Figures

Abstract

Clusters of galaxies are the largest objects to collapse under their own gravity and virialise. Cluster properties provide a unique way of constraining cosmological parameters. This is achieved using the mass function via the scaling relations. While the mass function can be directly related to the cosmology of the Universe, the scaling relations relate properties of clusters to their mass. The scaling relations are thus used to place clusters on the mass function by relating mass to another observational property.

The simplest model of predicting the scaling relations is the self-similar model. Observational data show, however, that the self-similar model is insufficient, requiring additional processes which are not gravitational in origin.

In this thesis, a new simulation has been studied to investigate the effects of these non-gravitational processes (specifically, feedback from active galactic nuclei) on the cluster scaling relations. The results from the scaling relations at redshift zero show a similar result to the observational data, in that the self-similar relations are broken. When examining the scaling relations at higher redshifts, the luminosity relations show an even larger departure from the self-similar predictions in both normalisation and slope. However, temperature and Y parameter relations show a slow tendency to the self-similar result in terms of the slope but not in the normalisation. Also found is a slight departure from self-similarity in the $M_{gas} - M_{\Delta}$ relation slope but not in the normalisation. I conclude that scaling relations can not all be self-similar, so a new model for the scaling relations is required.

University of Manchester,
David Boulderstone
Master of Science
07 March 2013

Declaration

No portion of the work referred to in this thesis has been submitted in support of an application for another degree or qualification of this or any other university or other institution of learning.

My thesis is based on data from the simulations run by the Virgo consortium specifically, Peter Thomas and Chris Short. I have also included work on cluster catalogues, produced by Dr. Scott Kay. These form the basis of my anaylsis. I have further used a small section of code provided by my supervisor, Dr. S. Kay, to estimate the Q parameter. The remaining work is my own.

David Boulderstone

Jodrell Bank Centre for Astrophysics

Alan Turing Building

The University of Manchester

Oxford Road

Manchester

M13 9PL

U.K.

Copyright

Acknowledgements

Firstly thank you to my supervisor, Scott Kay, who calmly and patiently helped guide me throughout the course of this degree. The time you gave me was greatly appreciated.

I would also like to thank all students in the East and West wing, who have been kind and welcoming, in particular Andrew Jones, Rachana Bhatawdekar and Nicholas Wrigley. A very very (it's not a typo Carl) special thank you to both Carl Roberts and Philipa Hartley, without their help none of this would have been possible. Finally and very importantly, thanks to my parents and family who supported me throughout this degree, it means a lot to me.

"It is far better to grasp the Universe as it really is than to persist in delusion, however satisfying and reassuring." - Carl Sagan

David Boulderstone

Jodrell Bank Centre for Astrophysics,

Alan Turing Building,

University of Manchester,

Oxford Road,

Manchester,

M13 9PL.

Supervisor: Dr Scott Kay

Advisor: Dr Patrick Leahy

Chapter 1

Introduction

1.1 Preface

This chapter is an introduction to galaxy clusters and their properties that describes how clusters are used to probe cosmology. The various methods of mass estimation for clusters are reviewed before introducing the mass function. The self-similar scaling relations are discussed in chapter 2, as they can be used with the mass function to constrain various cosmological constants, by linking observables with mass. Observational determinations are then shown, and it is found that the self-similar predictions for the scaling relations are incorrect. This means that there are other non-gravitational processes occurring in the cluster, which are significant enough to break self-similarity. In chapter 3, I explain the new cosmological hydrodynamical simulation, which will be used in chapters 4 and 5 to examine the scaling relations. Initially, my results will focus on clusters at redshift zero, to compare the results from the scaling relations to predictions of the self-similar model. Then I will allow the redshift to vary, enabling the study of the evolution of the scaling relations with time. This can be compared to the self-similar model, by removing the self-similar evolution from the scaling relations. If any evolution is found after the removal then the scaling relations can be said to be not self-similar

1.2 Clusters

The largest known gravitationally bound objects are clusters. The collapse of clusters are the largest overdensities in the initial density field. The formation of these clusters seems to follow a hierarchical model [Press and Schechter, 1974]. The formation of clusters has occurred through multiple hierarchical galaxy mergers, whereby galaxies collide and combine to form larger galaxies, and through accretion of smaller systems, driven by gravity and dominated by dark matter. As the dark matter component makes up most the mass of the cluster ($10^{14} - 10^{15}$ solar mass ($M_\odot$)), it follows therefore that the cluster formation is modelled as a dark matter collapse, from the initial cosmological conditions. This massive collapse occurred more recently than most galaxy formation. Clusters are identified at $0 <$ redshift (z) < 2 [Staniszewski et al., 2009] and are a much less common cosmological feature than the roughly 50 to 10^3 galaxies which reside within them, which form much earlier [Bouwens et al., 2010];[Coe et al., 2012].

To better model cluster formation, supercomputers have been used to generate large scale numerical and/or hydrodynamical simulations. These simulations currently model the behaviour and evolution of the dark matter component of clusters accurately. However, the self-similar predictions [Kaiser, 1986], for results from simulations, are not as accurate and tend not to agree with the observed values. Some of the processes involved in galaxy formation must change the state of the intracluster medium (ICM) to account for some of the shortcomings of this simple model. The processes which have been suggested to account for this are non-gravitational in origin. This makes the data from observations of clusters an ideal place to test our models of galaxy formation and their effects on the surrounding ICM.

1.2.1 Properties of clusters

Clusters can be observed in the X-ray and Optical/Near-Infrared spectrum. The features of which are outlined here.

The colours of galaxies in clusters viewed in the optical tend to be redder than

other galaxies at a similar redshift [Voit, 2005]. This implies that clusters of galaxies have a very low star formation rate. The stripping of the intergalactic gas from galaxies, when they enter the cluster, is thought to account for this. Other possible mechanisms include galactic mergers and feedback from active galactic nuclei (AGN). These factors add little to the hot (10^{7-8} K) and diffuse (electron density (n_e) 10^{-2}) ICM, which is originally heated by gravitational collapse. The high temperature suggests that no or little star-formation is possible, as lower temperatures are required for the birth of stars.

When clusters are viewed in the X-ray, the luminosity comes from the ICM trapped in the potential well of the cluster [Voit, 2005]. X-ray emission relies on the distance and the angular size of the cluster and the central body accounts for a large part of the X-ray luminosity. This X-ray emission is bremsstrahlung and it dominates the emission spectrum above 2keV, which is a typical ICM temperature. Below this, temperature emission lines dominate the emission spectrum. The extended X-ray emission makes clusters easy to spot, as most X-ray sources are point-like, and this allows for mass estimation of clusters.

1.3 Mass estimation

In this section the methods for measuring mass are outlined. Mass estimation is included here to show how to determine the mass function, which is useful as it can be used to link observable features of clusters to their mass. This can then be used to constrain cosmological parameters. Whilst easy in theory to perform, this is very expensive, and the solution of course is to use a simulation to generate the mass function and then, by using the scaling relations, find the cluster's mass.

1.3.1 Velocity dispersion

The virial theorem can be used to infer the virial masses of galaxies or clusters ($M_{\rm vir}$) from their dispersion velocities (σ). This is possible so long as the object in question

is spherical and in virial equilibrium,

$$2K_{\rm e} + U_{\rm g} = 0 \tag{1.1}$$

which simplifies to

$$\sigma^2 \approx \frac{GM_{\rm vir}}{R_{\rm vir}} \tag{1.2}$$

where $K_{\rm e}$ is the total kinetic energy, $U_{\rm g}$ is the total gravitational potential energy and $R_{\rm vir}$ is the virial radius. Early observations by [Zwicky, 1933] of Abell 1689 found higher than expected kinetic energy for the mass observed. This lead to the postulation that invisible matter existed in and around the galaxies. In fact, about 80% of the matter in the cluster is invisible. This 'missing' matter is called dark matter.

1.3.2 Hydrostatic equilibrium

By assuming that the ICM in clusters may be in hydrostatic equilibrium, a mass estimation can be taken. This estimation is good enough because it will provide a rough value for mass. By assuming hydrostatic equilibrium for a cluster, we find the relation,

$$\nabla P_{\rm eq} = -\rho_{\rm g}\Phi \tag{1.3}$$

where $\nabla P_{\rm eq}$ is the change in equilibrium pressure, $\rho_{\rm g}$ is the gas density and Φ is the total gravitational potential. [Chiu and Molnar, 2012] finds that this is an acceptable method of testing cluster mass, when compared to other methods.

1.3.3 Weak gravitational lensing

Weak gravitational lensing is another method to estimate the mass of clusters, first suggested by [Zwicky, 1937]. This technique, which was not possible until recently, is sensitive to the projected cluster's radius $r_\perp$ and the deflection angle of the deflected photons [Tyson et al., 1990].

This method of mass measurement often agrees with mass estimates from X-ray emission. Furthermore, the advantage of this method is that it doesn't require assumptions about the geometry or equilibrium state to be made. The astronomers who use this model [Shan et al., 2012] claim that future surveys (DES, LSST, KDUST and EUCLID) will be able to provide more effective mass estimations for more clusters and will be able to further constrain current cosmological models [Dietrich and Hartlap, 2010].

1.4 Cluster halo definition

A method of defining the mass of a cluster in a simulation or observation is called the spherical overdensity (SO). It is based on the spherical top hat model of collapse and assumes that most of the mass is found at centre of the cluster. The SO equation,

$$M(< r) = (4/3)\pi r^3 \Delta \rho_{\rm cr}(z) \tag{1.4}$$

is used to solve for M($< r$) is the total mass profile within radius r and $\rho_{\rm cr}(z)$ is the critical density at that particular redshift z. This then allows for the growth of dark matter spheres until the mean internal density is equal to a factor Δ times the critical density. Using the Friedmann equation,

$$\rho_{\rm cr}(z) = \frac{3H_0^2}{8\pi G} E^2(z), \tag{1.5}$$

where H_0 is the Hubble constant and $E(z)$ for a flat Universe is given by,

$$E^2(z) = \Omega_{\rm M}(1+z)^3 + \Omega_\Lambda \tag{1.6}$$

where $\Omega_{\rm M} = \rho_{\rm m}/\rho_{\rm cr}$ and $\Omega_\Lambda = \rho_\lambda/\rho_{\rm cr}$. The advantage of the SO model is that it is a simple way to define the mass and size of a cluster, which allows observed and simulated clusters to be compared easily [Hoekstra, 2007]. This comparison is done to see if simulated data on the mass matches up with observational data. If not,

the dynamical processes used in the simulation can be improved upon to better represent the growth and evolution of clusters. This in turn betters the use of the observational data as a probe of cosmology.

1.4.1 Press-Schechter formalism and the spherical top hat model

Here, a quick run through of how simulations can be used to compute the mass function, which can be used with the scaling relations to compare the cluster count to the observational cluster count.

[Press and Schechter, 1974] (PS) formalised the growth of structure as hierarchical linear growth of a density perturbation in the dark matter field. PS was the first to relate the spherical top-hat model collapse and the growth factor, which led to the semi-analytical method, using the cluster mass function to constrain the cosmological parameters [Eke et al., 1996].

The spherical top-hat collapse model evolves with respect to the top-hat radius [Gunn and Gott, 1972]. A one dimensional density perturbation with a radius R, a density ,ρ, an overdensity, δ, which is greater than zero, and a mass, M, modelled by

$$M = (4\pi/3)(1+\delta)\rho R^3 \tag{1.7}$$

The growth of the perturbation is defined by the growth equation, which comes from the idea that large scale structure in the Universe arises from small quantum fluctuations (perturbations) in the very early Universe, which are then enlarged during the inflation era. The overdensity,

$$\delta(x,t) \rightarrow D(t)\delta_0(x,t) \tag{1.8}$$

where D(t) is the linear growth factor. This shows that the small perturbations continue to grow in size and the areas where there are negative perturbations (underdensities) continue to shrink in terms of density, as redshift decreases. However,

as this growth is occurring, there is a slow decrease rate in radius. This behaviour continues until it reaches the turnaround epoch, the point at which the perturbations collapses and begins to virialise. The time-scales of the turnaround epoch are set by the initial conditions in which the perturbation formed. This growth effect gives rise to dark matter haloes, that form structure, and voids, which are empty regions in the Universe.

The critical density, the density at which the overdense regions form clusters, will give an indication of the number of haloes present in the Universe at that redshift. To measure this requires the use of simulations, which models a small box in the Universe. The simulation, which models cluster formation and evolution, uses the linear theory prediction which predicts $\delta_{\text{critical}} = 1.686$ for all redshifts. This can be used to compute the mass function at that particular redshift.

1.5 Cluster mass function

The cluster mass function describes the number of dark matter haloes (clusters) in unit volume and unit mass. This gives a measure of the number of clusters present in a Universe for a given cosmological model. The mass function's only variables are mass and redshift, which make it easy to compare simulated data with observational data.

Figure 1.1 shows that the mass function determines cosmology of the Universe. To use the mass function, we need observable quantities which link with mass, such as luminosity, temperature, gas mass etc, these links are called scaling relations.

In summary, cluster scaling relations are required to constrain cosmological parameters. We now go on to discuss the self-similar model, which outlines a simple model for the scaling relations.

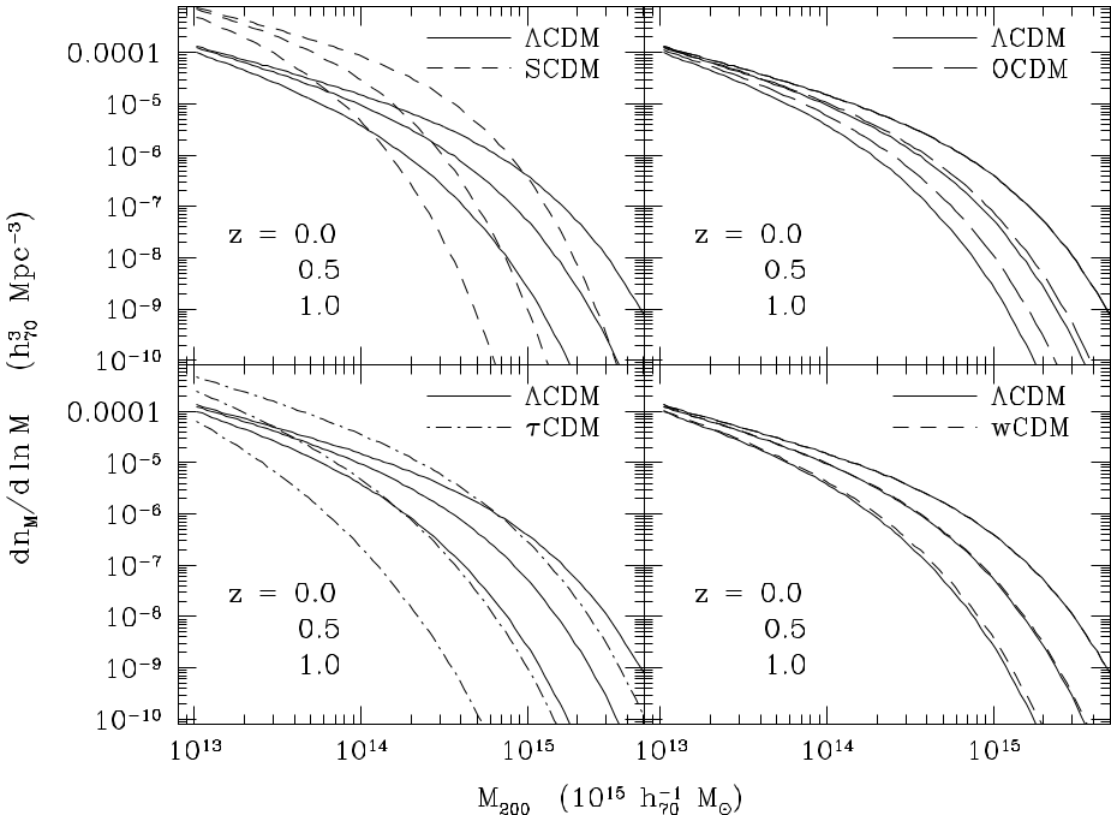

Figure 1.1: The mass function can be used to compare cosmological models. In each panel the ΛCDM model is compared against another competing cosmological model. In the top left is the standard cold-dark-matter model (SCDM), in the top right the low density model (OCDM), in the bottom left a fixed power spectrum model(τCDM), and finally in the bottom right is the dark energy model (wCDM) [Voit, 2005].

Chapter 2

Cluster scaling relations

2.1 Self-Similar model

The "self-similar" scaling relations were first described by [Kaiser, 1986]. They are useful because they provide a link between an observable quantity to mass and hence the scaling relations can be used with the mass function to constrain cosmological parameters.

The self-similar scaling relations developed by [Kaiser, 1986] are based on three key assumptions. The first assumption is that the Universe is an Einstein-de Sitter Universe, $\Omega_{\rm m} = 1$, and that the clusters have formed through gravitational collapse. The next assumption is that the initial perturbations present in the early Universe do not have a pre-set or preferred scale; this allows scale-free or self-similar perturbations (beyond gravitational collapse and shock heating), to evolve and grow. The final, and perhaps most interesting, assumption is that other physical processes, which shape the formation of clusters, do not interfere with formation nor do they introduce their own scaling into the model.

2.2 Derivation of the scaling relations

Below, cluster mass M_Δ is defined to be the mass in a spherically symmetric region with radius r_Δ which has a mean density, $< \rho >= \Delta\rho$.

$$M_\Delta = (4/3)\pi r^3 \Delta \rho_{\rm cr}(z) \tag{2.1}$$

Therefore,

$$r_\Delta \propto \left(\frac{M_\Delta}{\Delta E^2(z)} \right)^{1/3} \tag{2.2}$$

assuming the virial theorem, which relates kinetic energy $K_{\rm e}$ and potential energy U holds,

$$2K_{\rm e} + U = 0, \tag{2.3}$$

and for intra-cluster gas,

$$K_{\rm e} \propto T, \tag{2.4}$$

the temperature, T, scales with mass and radius as,

$$T \propto M_\Delta / r_\Delta \tag{2.5}$$

These equations will be used to derive the individual scaling relations.

2.2.1 Mass-Temperature relation

From equations 2.5 and 2.2, the temperature is predicted to scale with mass as:

$$T \propto (\Delta \rho_{\rm cr})^{1/3} M^{2/3}, \tag{2.6}$$

where T is the temperature measured within the radius R. Equivalently:

$$M \propto T^{3/2} E(z)^{-1} \Delta^{-1/2}, \tag{2.7}$$

the predicted value of the slope of the $M - T$ relation is 3/2. In the simulations the relation will be temperature-mass, so the gradient is just 2/3 for the self-similar model. Furthermore the temperature mass relation will be split up into two different components, the mass weighted temperature and the spectroscopic like temperature (see chapter 3 for more detail).

2.2.2 Luminosity-temperature relation

The bolometric X-ray luminosity, $L_{\rm X}$, is defined as,

$$L_{\rm X} = \int_V \epsilon(T(n))dV \tag{2.8}$$

where ϵ is the emissivity, V is volume and n is the gas density. If the particles only interact collisionally, then

$$\epsilon(T, n) = n^2\Lambda(T, Z) \tag{2.9}$$

where $\Lambda(T, Z)$ is a cooling function. Substituting this back into the equation 2.8 gives

$$L_{\rm X} = \int_V n^2\Lambda(T, Z)dV \tag{2.10}$$

Assuming the cluster is isothermal and $T \gg 10^7K$, giving $\Lambda(T, Z) \rightarrow \Lambda_0 T^{1/2}$, then the above expression can be rewritten as

$$L_{\rm X} = \Lambda_0 T^{1/2} \int n^2 dV. \tag{2.11}$$

Assuming a spherically symmetric cluster, the volume element $dV = 4\pi r^2 dr$ gives

$$L_{\rm X} = \Lambda_0 T^{1/2} 4\pi \int_0^{r_\Delta} n^2 r^2 dr. \tag{2.12}$$

Using $x = r/r_\Delta$ gives,

$$r^2 dr = r_\Delta^3 x^2 dx \tag{2.13}$$

Further assuming that $n(r) = \rho(r)/\mu m_{\rm H}$, where $\mu \simeq 0.59$ is the mean molecular weight of ionised gas, and $\rho(r)$ can be written as $\rho(r) = f(x)\Delta\rho_{cr}(z)f_{\rm gas}$, equation 2.12 can be rewritten as

$$L_{\rm X} = \frac{4\pi\Lambda_0 T^{1/2} r_\Delta^3 \Delta^2 \rho_{\rm cr}^2 f_{\rm gas}^2}{(\mu m_{\rm H})^2} \int_0^1 x^2 f^2(x) dx \tag{2.14}$$

For self-similar clusters the integral is a constant and the gas fraction, $f_{\rm gas}$, is independent of mass. This expression simplifies to the following scaling relation

$$L_{\rm X} \propto T^{1/2} r_{\Delta}^{3} \Delta^{2} E^{4}(z) f_{\rm gas}^{2}. \tag{2.15}$$

Using equation 2.2, we have

$$r_{\Delta}^{3} = \frac{M_{\Delta}}{E(z)^{2}\Delta}. \tag{2.16}$$

Substituting this back into equation 2.15 gives

$$L_{\rm X} \propto T^{1/2} M_{\Delta} E(z)^{2} \Delta f_{\rm gas}^{2}. \tag{2.17}$$

Using equation 2.7 this simplifies to

$$L_{\rm X} \propto T^{2} \Delta^{1/2} E(z) f_{\rm gas}^{2} \tag{2.18}$$

The prediction from self-similar model gives the slope of the L-T relation at 2. This can be compared to the observational data to see if the model matches.

2.2.3 Q parameter-mass relation

The integral in equation 2.14 is known as the Q parameter, which is a dimensionless emission measure, or clumping factor. This measures the effect of changes in the gas in density structure as a function of mass, which is related to the cluster's luminosity [Stanek et al., 2010]. For a self-similar clusters, Q is a constant. This is a theoretical relation and we are unable to compare this relation directly to observational data. However, it provides an interesting insight into the non-self similar structure of clusters.

2.2.4 Luminosity-mass relation

Starting from, the $L - T$ relation,

$$L_{\rm X} \propto T^2 \Delta^{1/2} E(z) f_{\rm gas}^2 \tag{2.19}$$

and using equation 2.6 gives

$$L_{\rm bol} \propto M^{4/3} \Delta^{7/6} E(z)^{7/3} f_{\rm gas}^2 \tag{2.20}$$

The gradient of the $L - M$ relation is, therefore, predicted to be 4/3.

2.2.5 Y parameter-mass relation

The $Y_{\rm SZ}$ parameter is the observable associated with the global thermal Sunyaev-Zel'dovich (SZ) effect [Zeldovich and Sunyaev, 1969], which is caused by the ICM's electrons interacting with the cosmic microwave background radiation (CMB). This interaction occurs through inverse Compton scattering, where the CMB photons gain energy from collisions with the electrons within the ICM. The resulting effect is a distortion of the CMB photons which can be used to locate density perturbations, such as clusters.

A related quantity, $Y_{\rm X}$ but based on X-ray data and the spectroscopic temperature, $Y_{\rm X} \propto T_{\rm X} M_{\rm gas}$, whereas the SZ version is $Y_{\rm SZ} \propto T_{\rm m} M_{\rm gas}$ and is based on the mass weighted temperature $T_{\rm m}$.

Beginning with defining Y,

$$Y \propto M_{\rm gas} T \tag{2.21}$$

and using $M_{\rm gas} = f_{\rm gas} M_\Delta$ gives

$$Y \propto M_\Delta f_{\rm gas} T. \tag{2.22}$$

Further, using

$$T \propto M_\Delta^{2/3} E^{2/3} \Delta^{1/3} \tag{2.23}$$

gives the $Y - M$ relation

$$Y \propto f_{\rm gas} M_{\Delta}^{5/3} E^{2/3} \Delta^{1/3} \tag{2.24}$$

which predicts the value of slope to be 5/3.

2.3 Observations

This section discusses the observed scaling relations. The observational data is used to test the self-similar model, to discover if the self-similar relations are an accurate representation of the cluster population. If the observational data disagrees with the self-similar model, which models gravity alone, then other, non-gravitational processes must be taking place inside the cluster's ICM.

Astronomers have used a variety of satellites to gather X-ray observational data, these are discussed below. When the observations took place is important, because that determines which satellite was used. Instruments on-board the satellites have improved over the years, so we may expect to see a change in the observed scaling relations as the equipment improves.

- *GINGA*, Japanese for galaxy, was an X-ray astronomy satellite which operated from 1987 to 1991. It contained the Large Area Proportional Counter, All-Sky Monitor and Gamma-ray Burst Detector.

- *ROSAT*, short for Röntgensatellit, was a German designed X-ray telescope, which was used between 1990 and 1999. *ROSAT* contained two Position-Sensitive Proportional Counter (PSPC), this instrument conducted an all sky survey in which many clusters were observed.

- *ASCA*, or Advanced Satellite for Cosmology and Astrophysics, was commissioned by Japan but the United States provided the scientific equipment, and was in use from 1993 to 2001. *ASCA* was the first satellite to use CCDs for X-ray astronomy, which greatly improved the observation results. *ASCA* could also measure temperatures of X-ray sources and so the *ASCA* satellite was widely used for these features.

- *Chandra* X-ray Observatory, *Chandra*, is an X-ray satellite which was launched in 1999. *Chandra* is a powerful X-ray source detector, finding X-ray sources about 100 times fainter than previous X-ray telescopes. The high resolution of *Chandra* also helped improve the quality of the observational data.

- $XMM-Newton$, X-ray Multi-Mirror Mission Newton, is an X-ray observatory launched by ESA in 1999. $XMM-Newton$ was used to perform a survey of cluster structure (REXCESS), which we will use to compare with our simulated data.

2.4 Summary of observed scaling relations

2.4.1 M-T data discussion

Value for the M-T slope	Error	Paper name
1.98	0.18	[Mohr et al., 1999]
1.94	n/a	[Neumann and Arnaud, 2001]
1.78	0.01	[Finoguenov et al., 2001]
1.74	0.09	[O'Hara et al., 2007]
1.65	0.26	[Zhang et al., 2008]
1.53	0.08	[Vikhlinin et al., 2009]
1.59	0.18	[Eckmiller et al., 2011]

Table 2.1: Observational data for the temperature-mass relation slope, with the self-similar result being 1.5.

Table 2.1 summarises various observational determinations of the slope of the $M-T$ relation, which we discuss below.

- [Mohr et al., 1999] studied 45 galaxy clusters' ICM temperature between 2.4−5 keV, using *ROSAT* (PSPC) data to determine the values for the $M-T$ slope. The paper includes the comparisons between the observational data and simulations of cluster structure formation and feedback from galactic winds in the ICM. The paper then goes on to acknowledge that their observed values for the scaling relations are steeper than the self-similar prediction.

- [Neumann and Arnaud, 2001], again using *ROSAT*(PSPC), examine a sample of clusters with $T > 3.5$ keV and at redshifts between $0.04 < z < 0.06$. These were taken from the Abell catalogue, which contains 4073 rich clusters of galaxies. This paper also finds that clusters break from the self-similar scaling of [Kaiser, 1986].

- [Finoguenov et al., 2001] fitted $M - T$ relations for two cluster samples. The first sample contained 63 clusters. The second, which was not flux limited, contained 88 clusters and was used as a comparison to the first sample in terms of the scaling relations. Both samples are from the *ROSAT* All-Sky Survey with *ASCA* used to find the temperatures of the X-ray sources. From these samples, the observed slope of the M-T scaling relation calculated differed from both the self-similar collapse predictions and hydrodynamical simulations.

- [O'Hara et al., 2007], using *Chandra*, studied a sample of 70 galaxy clusters at redshifts from 0.18 to 1.24. They then used observables from clusters which had their core subtracted. They found that excluding cluster cores results in a slope more consistent but still steeper than the self-similar model. They also find that both observed M-T relations evolves more than the slowly at high redshift than was previously predicted in the self-similar model [Kaiser, 1986].

- [Zhang et al., 2008] analysed 37 clusters at redshifts 0.14 to 0.3 from *XMM − Newton* data to compare with self-similar scaling relations. The paper finds that all relations based on the X-ray data are consistent the self-similar model.

- [Vikhlinin et al., 2009] used 42 clusters at temperatures above 4.5 keV from *Chandra*, which were first identified from the *ROSAT*(PSPC) All-Sky survey. Then they measured the evolution of the scaling relations with redshift. They find that their results agree with the self-similar model with minor corrections.

Value for the L-T slope	Error	Paper name
3.37	0.004	[David et al., 1993]
2.64	0.27	[Markevitch, 1998]
2.88	0.27	[Arnaud and Evrard, 1999]
2.47	0.14	[Ikebe et al., 2002]
2.35	0.33	[O'Hara et al., 2007]
2.70	0.24	[Pratt et al., 2009]
2.52	0.10	[Eckmiller et al., 2011]
2.51	0.29	[Maughan et al., 2012]

Table 2.2: Observational data for the luminosity-temperature relation slope, with the self-similar result being 2.

2.4.2 L-T data discussion

Table 2.2 summarises various observational determinations of the slope of the $L-T$ relation, which we discuss below.

- The [David et al., 1993] value came from 104 clusters and is interesting as this value differs greatly from the self-similar model and has a very low error. In this paper they challenged the value of the $L-T$ slope made by [Kaiser, 1986] and pointed out that the data gathered so far [Edge et al., 1990] by the satellites at the time ($ROSAT$ and $GINGA$) disagreed with his scaling relations. He also stated that there is a decrease in the X-ray luminosity of clusters measured above redshift 0.06.

- The [Markevitch, 1998] value for the $L-T$ slope was gathered by using $ROSAT$ for temperatures of 3.5 to 10 keV, which were measured by $ASCA$, and this paper's value was much closer to the expected value. They stated that their value for the slope could be compared to models of the scaling relations which do not include radiative cooling.

- [Arnaud and Evrard, 1999] studied 24 clusters that came from $GINGA$, and showed an absence of strong cooling flows. Both cool core cluster and non cool core clusters were sampled to investigate whether the steepening of the $L-T$ relation was caused by the morphology of the cluster.

- [Ikebe et al., 2002] used 61 galaxy clusters with temperatures of 1.4 to 11 keV

from the *ROSAT* data - again *ASCA* was used to measure their temperatures - to estimate the scaling relations. They find a close fit to the self-similar model.

- [Pratt et al., 2009] studied 31 clusters from the $XMM-Newton$ Cluster Structure Survey (REXCESS), which extends to lower mass clusters with its improved resolution. He used temperatures between 2 to 9 keV and there was no bias towards cluster morphological type. The results contained slopes which were also much steeper than the [Kaiser, 1986] self-similar values and they claimed this was due to the robust non-biased approach, because cool core and morphologically disturbed clusters were included in the results.

- [Eckmiller et al., 2011] recognised that a break in the self-similar model exists due to the effects of non-gravitational processes. The goal of this paper was to test this break on 26 clusters and groups and attempt to find the most reliable mass estimate for future research. Using the *Chandra* satellite again, a steepening in the $L-T$ slope is found for $T < 3$keV. However, the paper then states that only a small change is found for the other relations and that this does not have a strong effect on the self-similar scaling relations. His values agreed with the expected values from the self-similar model.

- [Maughan et al., 2012] used data from *Chandra* satellite and REXCESS at redshifts between 0.1 and 1.3. Then they divided clusters by morphology, cool core clusters and non-cool core clusters, to test the effect of cool cores on the scaling relations. They found that in the most gravitationally relaxed clusters the self-similar model holds true. However, using REXCESS data, the results indicated that the self-similar relations for the most relaxed clusters and non cool core clusters break at a temperature of 3.5 keV, dropping below the self-similar value for the slope. Interestingly, the cool core and unrelaxed clusters also break the scaling relations, as they appear to have a steeper slope then the self-similar model. The paper then suggested that this is due to non-gravitational heating in the form of central heating with entropy enhancements from galaxy merger shocks (see the next section).

2.4.3 L-M data discussion

Value for the L-M slope	Error	Paper name
1.84	0.09	[Reiprich and Böhringer, 2002]
1.90	0.49	[Maughan et al., 2006]
1.63	0.08	[Maughan, 2007]
2.33	0.70	[Zhang et al., 2008]
1.90	0.11	[Pratt et al., 2009]
1.44	0.06	[Eckmiller et al., 2011]

Table 2.3: Observational data for the luminosity-mass relation slope, with the self-similar result being 1.33.

Table 2.3 summarises various observational determinations of the slope of the $L - M$ relation, which we discuss below.

- [Reiprich and Böhringer, 2002] used the *ROSAT* All-Sky Survey and PSPC to model the ICM density profile of 106 clusters. They used the X-ray luminosity to find the $L - M$ relation and produced some cosmological constraints. The paper suggested that the values differ from the scaling relations due to possible systematic uncertainties and attempts to solve for them. However, the paper did not resolve these systematics, so necessarily their final value remains different to the self-similar value.

- [Maughan et al., 2006] examined 11 clusters, observed with $XMM-Newton$ and/or *Chandra*, at high redshift, $0.6 < z < 1.0$, and found that the scaling relations strongly disagree with the self-similar prediction, suggesting that non-gravitational heating, is occurring at redshift 1 or higher, and this is responsible for the steepening of the relations.

- [Maughan, 2007] analysed, using $XMM-Newton$ and/or *Chandra*, 115 clusters from a large range of redshifts, $0.1 < z < 1.3$, to probe the scaling relations. The results suggested that cluster masses, estimated from simple luminosity measurements, are inaccurate. The paper accounted for this by excluding the cores of clusters from the observational data, and found that the scaling relations were closer to the self-similar model.

- Results from [Zhang et al., 2008], [Pratt et al., 2009] and [Eckmiller et al., 2011] are discussed in sections 2.4.1 and 2.4.2.

2.4.4 Summary of observed slopes

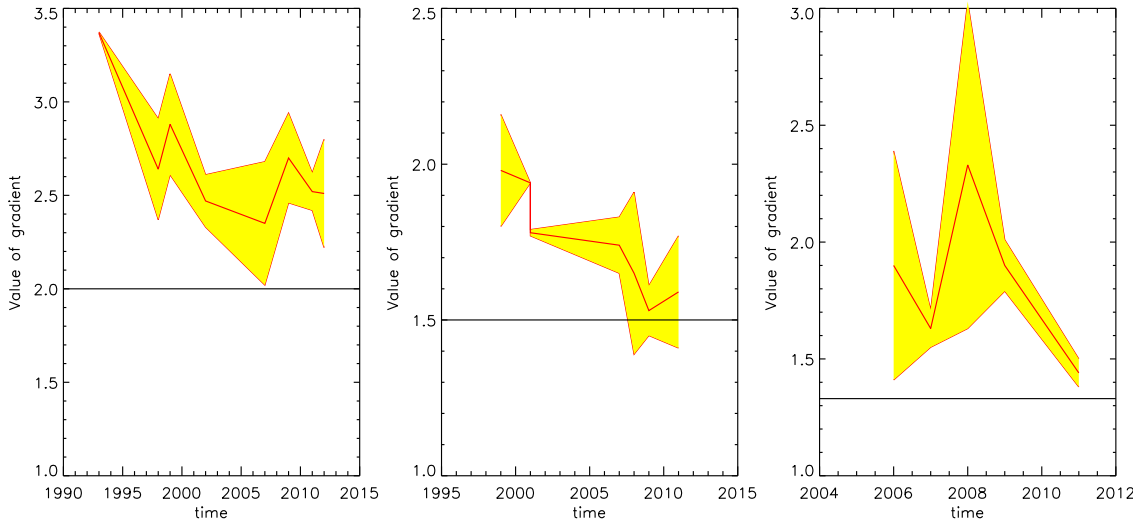

Figure 2.1: The central red line in all three graphs is the observed gradient of the scaling relations over time, with the self-similar model plotted as a solid black line for comparison. The yellow shading represents the error of each point. The left panel shows the $L-T$ relation, the middle panel shows the $M-T$ relation and the right panel shows the $L-M$ relation.

It is clear from figure 2.1 that the observed values for the slope of the $L-T$ scaling relation have never been in agreement with self-similar model, whereas recent observations of the $M-T$ relation are closer to self-similar model after some time, and that the $L-M$ relation did not match self-similar model. Many of the observations excluded cluster cores producing results closer to the self-similar model.

2.5 Self-similarity breaking

The observed scaling relations are not self-similar, as seen from observational data, especially for luminosity and when cluster cores are included. This suggests that non-gravitational heating processes affect the ICM. Such processes can be explored with cosmological simulations to test whether the modified scaling relations agree with observational data.

2.5.1 Non-gravitational processes

The observational data points to a non-gravitational process increasing the entropy of the ICM. This entropy is the cause of the break in self-similarity [Voit et al., 2005]. Possible mechanisms by which entropy is introduced into the ICM are pre-heating, radiative cooling, supernovae feedback and AGN feedback. These mechanisms are included in simulations (e.g. see [Borgani et al., 2006] and [Kravtsov et al., 2006]). However, due to the computational expense, it is only recently that a detailed computational study of clusters with these mechanisms has been possible.

The first method of accounting for entropy is assuming some sort of pre-heating occurred at an earlier epoch for all clusters [Kaiser, 1991];[Evrard and Henry, 1991]. This introduces a minimum level of entropy before the ICM collapsed into the cluster's gravitational potential well. This implies that there must be fairly high entropy at the cluster's core that is more significant in low mass systems. This minimum level produced a better value for slope of the $L - T$ relation. However, [Böhringer et al., 2002] showed, using X-ray data from $XMM - Newton$, that there is a deficiency in the expected cool cores in host galaxies. Also, as shown by [Shang et al., 2007], the Lyα absorption lines push the time when preheating can occur into only very high redshifts, which means that the pre-heating model could not have enough time to heat the gas, unless pre-heating only occurred in the most dense regions of the intergalactic medium.

Radiative cooling was originally suggested by [Bryan, 2000] to fix the entropy problem. Radiative cooling removes the low-entropy gas from the ICM and leaves the high entropy gas with a longer cooling time, to be observed in X-rays. This provides an accurate picture of the entropy and is supported by hydrodynamical simulations [Pearce et al., 2000];[Muanwong et al., 2001];[Ettori and Brighenti, 2008]. Unfortunately, radiative cooling converts too large a fraction of ICM into stars, and most observations of clusters suggest that only a small amount of the total baryonic content is in stars [Balogh et al., 2001]. Another problem with radiative cooling is that it quickly increases the ICM temperature at the centre of clusters [Borgani et al., 2004].

Supernovae driven winds could account for the entropy seen in the ICM [Metzler and Evrard, 1994] [Davé et al., 2008]. However, the sheer amount of energy required to heat the ICM to the required level is far too large to be provided by supernovae feedback [Kravtsov and Yepes, 2000]; [Kay et al., 2004], as almost all of the supernovae energy would have to be converted directly into thermal energy.

AGN feedback is due to accretion of the ICM onto the supermassive black holes; this has an observed effect on clusters [McNamara and Nulsen, 2007]. The energy generated by AGN accretion is enough to heat the ICM to nullify the effects of cooling. AGN heating is responsible for keeping the gas warm in clusters containing cool cores, which should otherwise cool to lower the temperature quickly, because the high density gas in the centre of the cool core clusters has a short cooling time. AGN are also thought to quench star formation in clusters and to provide hot gas fractions found in the centre of clusters [Sun, 2008].

AGN, however, do have problems which need to be understood. Some of the first models show jets from AGN forming bubbles of hot gas/plasma. However, these superheated plasma bubbles do not appear to being expanding fast enough to account for the heat of the ICM; worse still, the bubbles seem to be the same temperature as the ICM. Also, if AGN heat only the centre of a cluster then, with strong AGN feedback, the cluster should have a flat entropy gradient. This would indicate that heat is moving away from the cluster's centre. However, this is not the case, as observations disagree [David et al., 2001]. Another problem is that at large radii, the amount of AGN feedback predicted is greater than what is currently observed [Voit et al., 2005]. These are problems of AGN feedback that need to be worked out, if AGN feedback is to be included in the new simulations. However, due to its energy output, AGN feedback must be included in the simulations of cluster core regions, cool cores, and the ICM, for at least smaller mass clusters.

Scaling relations from models that attempt to account for these dynamical processes are known as modified scaling relations. Modified scaling relations may depend on the redshift at which these dynamical processes take place. Such modifications may also be seen in the redshifts evolution of cluster scaling relations.

Chapter 3

Cosmological simulations of clusters

3.1 Outline of Simulations

The purpose of this chapter is to outline how the simulations are performed and how cluster properties are measured. Firstly, the physics going into the simulation is explained, which include gravity, hydrodynamics and other processes such as radiation cooling, star formation and feedback. Next, the methodology of the simulation is presented; this includes the initial conditions, time-stepping, softening and a basic flowchart of the simulation. Finally, the Millennium Gas simulations are described, including the various parameters for the cosmology of the Millennium Gas simulations, the halo finder used, and how the cluster properties are obtained. This outline is intended to inform the reader about how current simulations work.

3.2 Simulations

Simulations are used to test our understanding of cosmological structure formation; here they are specifically used to study clusters in a cosmological context. In these simulations, complicated effects inside clusters such as mergers, where galaxies inside the clusters collide, and other physical processes are modelled directly. This can

be used to test theories about the mass function and the scaling relations (see chapter 2). The upcoming sections introduce the different aspects of the methods used to simulate clusters and their properties. These include N-body simulations, hydrodynamics, semi-analytics, halo finders and the generation of cluster properties and catalogues.

3.3 N-body Simulations

Cosmological N-body simulations are used to analyse the development of non-linear, perturbations in the density field and the behaviour of large scale structure formation. These simulations are used to test models of structure formation. If the simulation or model is incorrect, then they can be refined, so our models and simulations can more accurately reflect reality.

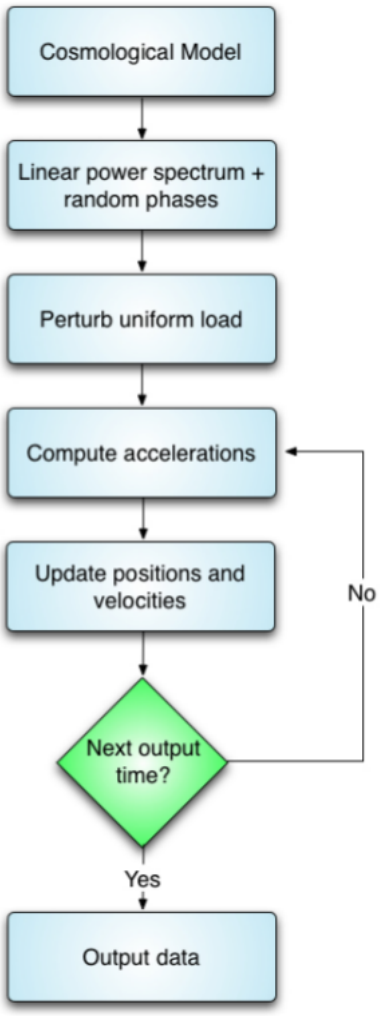

Figure 3.1: An overview of N-body simulations [Kay, 2013].

The simulation starts with a set of initial conditions (see figure 3.1), these are normally set by a cosmological model. These start with an unperturbed distribution of N points, referred to as particles. These particles are placed into a cube with periodic boundary conditions applied to satisfy the cosmological principle. The particles are perturbed using an input power spectrum. Then the gravitational force calculations are done, usually in co-moving co-ordinates. Finally, the integration of accelerations and velocities of the particles are done at each timestep (Δt), chosen such that,

$$\Delta t = \alpha\sqrt{\epsilon/|\ddot{x}|} \tag{3.1}$$

where α is a parameter which affects the accuracy of integration of the particles, ϵ is the gravitational smoothing coefficient (this reduces the likelihood of the particles from scattering off one another when in close proximity) and $\ddot{x}$ the acceleration of the particles, found by solving the equation of motion:

$$\ddot{x} = -2H\dot{x} - \frac{1}{a^2}\nabla_x\delta\phi \tag{3.2}$$

where H is the Hubble parameter, $\dot{x}$ the velocity of the particles, $a = 1/(1+z)$ and $\delta\phi$ the gravitational field strength. The calculation of the acceleration $\ddot{x}$ can be done with several different methods: direct summation, particle-mesh method and/or oct-tree.

- Direct summation is the sum of the contributions from all the particles in the simulation. However, it is computationally expensive, scaling as the number of particles squared.

- Particle-mesh method uses a cubic mesh and solves the Poisson equation to compute the movements of the particles in the simulation.

- Finally an oct-tree breaks up the simulation into boxes and solves for each particle group inside, ignoring details inside distant particle groups.

It is through these methods or some combination thereof that the growth and evolution of dark matter haloes are modelled in a simulation. These haloes are expected

to mimic those in reality, however these methods do not model the gas physics present in galaxy and cluster formation. The solution is to include hydrodynamics.

3.4 Hydrodynamics

Hydrodynamical simulations are able to simulate both the dark matter and the gas. The dark component is simulated using the N-body method and the gas is added into the simulation, whose motion is solved by treating it as a fluid. The equation to solve for the gas physics is a modified Euler equation:

$$\frac{\delta \mathbf{v}}{\delta t} + (\mathbf{v}.\nabla)\mathbf{v} + \frac{\nabla P}{\rho} + \nabla\phi = 0 \tag{3.3}$$

where $\mathbf{v}$ is the velocity vector of the gas, t is time, P is gas pressure, ρ is gas density and ϕ is the gravitational field strength. Two different methods for solving this are mesh codes and smoothed particle hydrodynamics.

Mesh codes treat the gas as a fluid and find its properties on a system of fixed points. This code has well-defined boundary conditions, can adequately capture shocks and fluid discontinuities and can be adaptive, if necessary, in the simulation. However, it does not conserve momentum well, due to the fact that the properties of particles must be evaluated on a fixed grid.

Smoothed particle hydrodynamics calculates the fluid properties using a set of particle. This is done by smoothing the particles with a kernel,

$$\langle A(\mathbf{r})\rangle = \int A(\mathbf{r}')W(|\mathbf{r}-\mathbf{r}'|,h)\mathrm{d}^3\mathbf{r}' \tag{3.4}$$

where $\langle A(\mathbf{r})\rangle$ is the estimated quantity at particle position $\underline{\mathrm{r}}$, W is a kernel, h is a chosen width and the integral is performed over all other points,$\underline{\mathrm{r}}$. One example is a Gaussian window function with $h = \sigma$. This allows for a solution which is adaptive, fast, memory efficient and has no preferred direction. Unfortunately, this solution does not have well-defined boundary conditions and it models gas shocks less well. Instead, kernels with compact support (such as spline kernels) are used. The sum

is then performed over a fixed number of neighbours.

Equation 3.3 is adequate for following the initial collapse and accretion of gas in clusters. However, radiative cooling is required to properly simulate the formation of galaxies and clusters. The inclusion of feedback is also important and is included in the simulation used in this work. Unfortunately, much of the other physics is not well modelled. This is due to the low resolution of the simulation, which prohibits detailed modelling of star formation, within galaxies.

3.5 Semi-analytic models

Semi-analytic models can also be used to simulate clusters, but are not used in the results presented here. These semi-analytic models are very efficient at generating large amounts of galaxies, by using a dark matter halo merger tree. When using a halo merger tree a cluster's gas physics, dark matter component and satellites can be traced back through time, in the simulation.

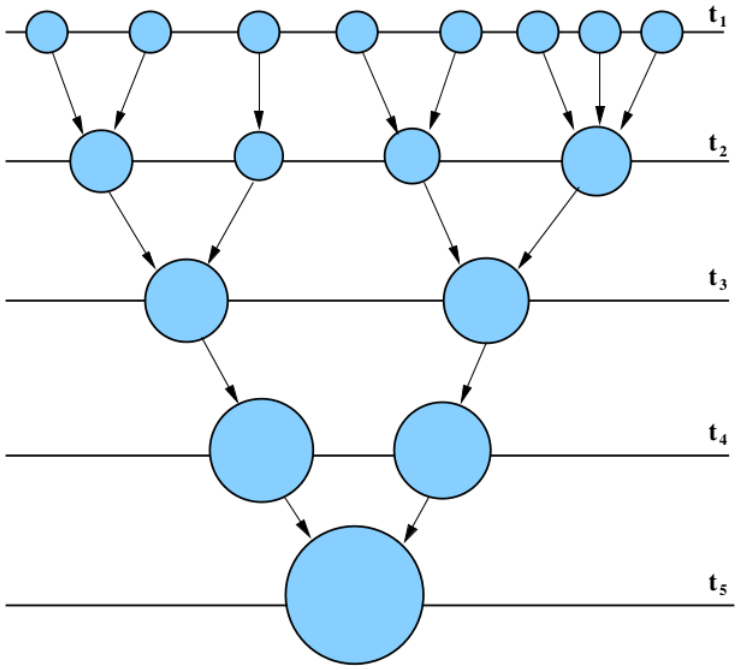

Figure 3.2: Example of a dark matter halo merger tree [Baugh, 2006].

A basic outline of a semi-analytic model is as follows:

- Input a cosmological model, with cosmological parameters.

- Then the dark matter halo merger trees are constructed.
- The gas physics are then run through. These processes include gas cooling, galaxy mergers, star formation, feedback, star bursts, chemical evolution, stellar populations and dust extinction [Cole et al., 2000].
- The galaxy and cluster observables can now be created.

3.6 Halo Finders

The haloes in simulations are found using three methods: Friends of friends, SUBFIND and spherical overdensity. These are now discussed.

3.6.1 Friends of friends

The Friends of Friends (FoF) algorithm, has historically been used to define haloes in simulated data [Press and Davis, 1982]. The FoF algorithm works by taking two particles from the simulation and grouping them, so long as they are separated by no more then a set length. This set length is known as the linking length. This process is then repeated on all the particles in the groups, until there are no more "friends" of particles with separation less than the linking length left. This process is favourable because there is only one parameter to set, the linking length, which does not assume any given shape for the dark matter halo.

However, the FoF algorithm is unsuccessful at determining the different subhaloes inside a large halo, which would be useful as these subhaloes can be galaxies or clumps of dark matter moving through the ICM of a cluster. Nor is it efficient at separating haloes from each other, as some particles in one halo may have "friends" in another halo, which leads to some clusters lying within one another. This problem increases with redshift which leads to questionable values for some cluster mass estimates [More et al., 2011]. It is for this reason that other methods of mass estimation are used, so that a comparison can be made to verify the FoF mass estimation.

3.6.2 SUBFIND

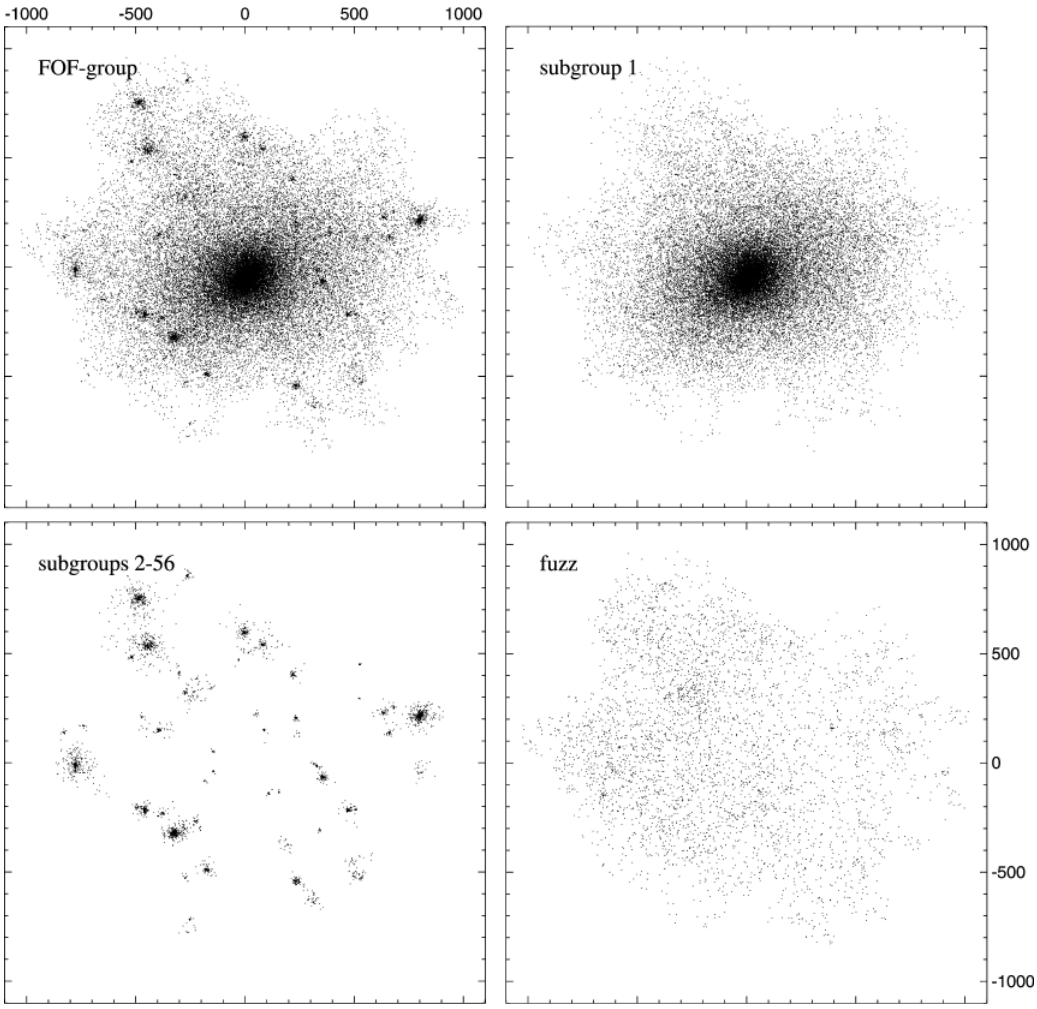

Figure 3.3: This figure shows an example output of the SUBFIND program. The top left panel is a friends of friends group identified as a cluster, the top right panel is the cluster with sub haloes removed, the bottom left is the sub haloes only, and the bottom right shows particles which are not bound to any subgroup [Springel et al., 2001].

SUBFIND is a program which separates out substructure from FoF groups. Within simulations, a substructure is a local overdensity, self-bound particle group within a parent group [Springel et al., 2001]. This removal is done by considering the most bound particle group, the input group, and comparing it with others in the FoF group. For all particles in the input group, a local estimate of the density at their positions is computed. This is done by setting the local smoothing scale to the distance of the nearest neighbour particle, then kernel interpolation is used to estimate the density over these neighbours. SUBFIND then ranks them in order

of decreasing binding energy, with subgroup 0 being the main cluster, and the remaining being substructure. This procedure allows the centre of the clusters to be accurately measured.

3.7 Cluster catalogue generation

To generate a cluster catalogue, the FoF algorithm is first used. This finds the dense regions of dark matter in the simulation. This is then passed to SUBFIND. A sphere radius r is then placed the centre of subgroup 0. This sphere is then grown until the total mass (M_Δ) in radius (r_Δ), is found whose mean density is $\Delta \cdot \rho_{cr}$. Where the critical density $\rho_{cr}(z)$, is

$$\rho_{cr}(z) = \rho_{cr,0} \cdot E(z)^2 \tag{3.5}$$

The value of Δ defines each of our catalogues. By setting a size and radius for the clusters enabling analysis of the clusters in the simulation, relationships can then be drawn between cluster mass and observables. We study several values, see table 3.1.

Label	Δ	Reason for inclusion
A	$\Delta_v \sim 100$	Virial radius from SO model[a]
B	200	Alternative to A
C	500	Observer data[b]
D	1000	Observer data[b]
E	2500	Observer data[b]
F	180	Alternative to A[b]

Table 3.1: Explanation for catalogue choices are as follows:
[a] Virial radius from the spherical top-hat model, using the formula from [Bryan and Norman, 1998].
[b] Cluster properties are more easily observed at this choice of Δ so comparisons to simulated data are easily done.

3.8 Estimation of cluster properties

Once the haloes have been found, calculating their bulk properties can occur. For particles within r_Δ observable and structure properties are calculated by assuming $\int dV\rho^n \rightarrow \sum_i m_i\rho_i^{n-1}$ [Stanek et al., 2010], where V is the volume of the cluster, ρ is the gas density of particle i and m_i is its mass. In this way we can estimate the following properties as:

- $L_{\rm bol}$, the bolometric X-ray luminosity, is calculated as

$$L_{\rm bol} = \int_V dV\rho^2\Lambda(T) \rightarrow \sum_{i=1}^{N} m_i\rho_i\Lambda(T_i) \tag{3.6}$$

  where $\Lambda(T)$ is the cooling function [Sutherland and Dopita, 1993] and T_i the temperature of gas particle i. Only then gas particles with $T_i > 10^6$K are considered.

- The mass weighted temperature, $T_{\rm m}$ is calculated as

$$T_{\rm m} = \frac{1}{M_{\rm gas}}\int_v dV\rho T \rightarrow \frac{1}{M_{\rm gas}}\sum_{i=1}^{N} T_i m_i \tag{3.7}$$

  where $M_{\rm gas}$ is the mas of hot gas in the cluster. Since m_i is a constant, $T_{\rm m}$ is therefore an average of the temperatures of the particles in a specific halo.

- The spectroscopic-like temperature, $T_{\rm sl}$, is calculated as

$$T_{\rm sl} = \frac{\int \rho^2 T_i^{1/4} dV}{\int \rho^2 T^{-3/4} dV} \rightarrow \frac{\sum_{i=1}^{N} m_i\rho_i T_i^{1/4}}{\sum_{i=1}^{N} m_i\rho_i T_i^{-3/4}}, \tag{3.8}$$

  following [Mazzotta et al., 2004]. The spectroscopic temperature is useful since it closely matches the X-ray temperatures from the observational data, for clusters with a kT $>$ 2keV.

- The global thermal SZ signal, $Y_{\rm SZ}$, parameter is calculated in the following

way,

$$Y_{\rm SZ} = \frac{k_{\rm B}\sigma_{\rm T}}{m_{\rm e}c^2}\int_v dV n_{\rm e}T_{\rm e} \rightarrow \frac{k_{\rm B}\sigma_{\rm T}T_{\rm m}M_{\rm gas}}{\mu_e m_{\rm H}m_{\rm e}c^2} \tag{3.9}$$

where $M_{\rm gas}$ is the mass of the gas in the cluster, $T_{\rm m}$ is the mass weighted temperature, $m_{\rm H}$ is the mass of a hydrogen atom, $k_{\rm B}$ is Boltzmann's constant, $\sigma_{\rm T}$ is the Thomson cross-section, μ_e is the mean molecular weight per free electron and $m_{\rm e}$ is the electron mass. We also calculate $Y_{\rm X}$, by replacing $T_{\rm m}$ with $T_{\rm sl}$.

- Following [Stanek et al., 2010] the clumping factor, Q, which is the effect of variations in density structure upon the halo luminosity, is defined as:

$$Q = \frac{1}{V}\int f^2(x)dx \rightarrow \frac{V}{M_{\rm gas}^2}\sum_{i=1}^{N} m_i\rho_i \tag{3.10}$$

where $x = r/r_\Delta$ and $f(x) = \dfrac{\rho(x)V}{M_{\rm gas}}$.

Now we shall discuss the simulation which was used to generate the data presented in the chapters that follow.

3.9 Scaling relations investigated

In the next two chapters, results from the simulated data will be presented, with the scaling relations for the most part being versus mass. These relations are the most relevant for cosmology. Included are relations which examine outcore clusters where we have removed cores ($r > 0.15r_\Delta$). These are included so that the effects of the clusters' core can be analysed.

Scaling relation	Note	Self-Similar slope
$L_{\rm bol}$ vs M_Δ	Bolometric	4/3
$L_{\rm boloutofcore}$ vs M_Δ	$L_{\rm bol}(r > 0.15r_\Delta)$	4/3
$T_{\rm m}$ vs M_Δ	Mass weighted temperature	2/3
$T_{\rm sl}$ vs M_Δ	Spectroscopic-like temperature	2/3
$T_{\rm sloutofcore}$ vs M_Δ	$T_{\rm sl}$(r> $0.15r_\Delta$)	2/3
$M_{\rm gas}$ vs M_Δ	$M_{\rm gas}$ = hot gas fraction $\times$ ${M_\Delta}^b$	1
$Y_{\rm X}$ vs M_Δ	X-ray $Y_{\rm X} \propto M_{\rm gas}T_{\rm sl}$	5/3
$Y_{\rm SZ}$ vs M_Δ	SZ $Y_{\rm SZ} \propto M_{\rm gas}T_{\rm m}$	5/3
Q vs M_Δ	Clump factor^b	0
$L_{\rm bol}$ vs $T_{\rm sl}$	Important for evolution^a	2
$L_{\rm bol}$ vs $T_{\rm sloutofcore}$	For completion^a	2
$L_{\rm boloutofcore}$ vs $T_{\rm sloutofcore}$	Out of core regions^a	2

Table 3.2: Individual scaling relations that will be investigated. All luminosities are in X-ray and bolometric.
^{a} These scaling relations are important for discussion in the evolution section.
^{b} These relations are unlike the others as they do not link an observable with mass; instead these relations link structural proprieties to mass. These relations are included for analysis of the cluster's structure.

3.10 New Millennium Gas Simulation

Results in this thesis are from the New Millennium Gas Simulation (NMGS) which is based on the earlier Millennium Simulation (MS) and Millennium Gas Simulations (MGS).

The original Millennium simulation, MS, was a dark matter only N-body simulation ([Springel et al., 2005]), which used the WMAP 1 cosmology ($\Omega_{\rm m} = 0.25$, $\Omega_\Lambda = 0.75$ and $\sigma_8 = 0.9$). It used a 500Mpc/h box, and 2160^3 dark matter particles. The galaxy properties were generated using a semi-analytic galaxy formation models [Guo et al., 2011].

The MGS [Stanek et al., 2009];[Hartley et al., 2008];[Kay et al., 2012];[Short et al.,

2010] had the same initial conditions as the MS, which includes the same haloes forming. However, it had lower resolution. The MGS also had the same box size and cosmology as the MS but it included gas physics (5×10^8 dark matter particles and 5×10^8 gas particles). Three versions of the MGS were run: a gravitational only (GO) run, a preheating (PC) run which included heating from stars and supernovae and cooling, and a model containing feedback (FO) from galaxies.

The NMGS had different initial conditions following the WMAP 7 cosmology ($\Omega_{\rm m} = 0.27$, $\Omega_\Lambda = 0.73$ and $\sigma_8 = 0.81$). It was run with two different box sizes, a 500Mpc/h box and a 250Mpc/h box, and its resolution was approximately the same as the MS, with 1×10^{10} dark matter particles. It also utilised a feedback only (FO) model, including AGN feedback, which worked by:

- First running the dark matter only simulation, which generates the halo catalogues (galaxies and clusters).
- Next a semi-analytic model is run on the haloes, which involves merger trees to calculate the feedback from each galaxy (AGN, supernovae and metals).
- Finally the simulations are rerun with gas and uses the feedback tables to inject energy into the gas in haloes. A caveat; the gas gravitational effect is ignored, therefore, the dark matter particles alone determine the size and position of the haloes.

Full details of the model can be found in [Short et al., 2013].

3.10.1 Data Selection

Finally, this section outlines how I selected the clusters from the NMGS for my analysis.

- A mass limit was imposed, so that only the most massive clusters were found by my program. The minimum selected mass was $1 \times 10^{14} {\rm M}_\odot$ and the maximum was $2 \times 10^{15} {\rm M}_\odot$. The maximum limit was only imposed so that no data with erroneously high mass could be part of the data analysis.

- Through the use of SUBFIND, only subgroup 0, i.e. the parent group, is selected for data analysis, the catalogues also store the other massive subgroups.
- A temperature minimum (2.0 keV) was used so that clusters emitting only in bremstrahlung radiation were selected for data analysis. This removed a group of anomalous clusters which were skewing the co-variance matrix, see chapter 4. It is also require for accurate calculation of $T_{\rm sl}$.
- Use of minimum hot gas fraction was imposed, f_{gas} 10%, so as a handful of erroneous objects appeared in the data, which had very low gas fractions. This filters them out.

Once the selections had been processed, the analysis of the mass function and the scaling relations can begin.

3.10.2 Mass function from the NMGS

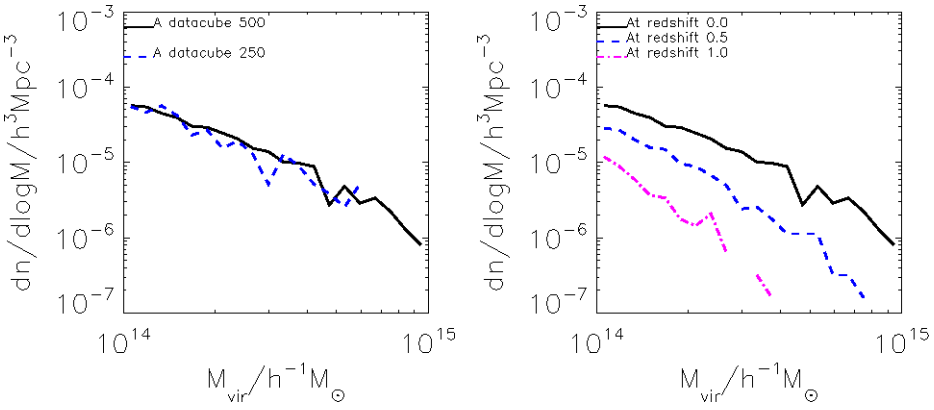

Figure 3.4: The graph shows two mass functions taken from the NMGS; the left panel shows the mass function at various redshifts and the right shows a comparison of different box sizes, at redshift zero.

Shown in figure 3.4 are the cluster mass functions of the NMGS, determined by taking dark matter haloes which have masses of $10^{14} - 10^{15} M_\odot$, to ensure a mass function containing clusters only. The right panel shows that the redshift scales inversely with the number of clusters, because of the collapse time-scale. This means that clusters form near the end of the simulation. When comparing this to

observations, clusters have only been observed relatively recently at $z = 0 - 2$, so this matches the expectation, qualitatively.

The left panel just plots a larger simulated box size (500Mpc/h) on top of another simulated box which is half the size (250Mpc/h), both box sizes are at redshift zero. The larger simulated box size is less noisy, as it contains a larger number of clusters than the smaller simulated box. This shows that the 500Mpc/h box is a more effective place to draw the cluster scaling relations from, since the data will produce statistically more robust results.

Chapter 4

Scaling relations at redshift zero

This chapter is concerned with the scaling relations obtained from the NMGS, primarily focused on the relations that scale with mass; beginning with a brief explanation of the code methodology. One important detail is describing how the fit parameters, α, β and σ, and their associated errors are found. These are broken down into fitting the normalisation, α, and slope, β, of the relations, scatter, σ, analysis and error estimation. Then the main results at redshift zero are shown, for different density contrasts. Afterwards, the scaling relations are compared to each other through a correlation analysis, using Pearson's coefficient. Finally the relations are compared to observational data, to see if the results are similar.

4.1 Methodology

This section is a brief overview of the methods used in the code written to analyse and extract the best-fitting parameters describing the scaling relations. This is shown so that the tables and graphs in the later sections have context, as discussion of the technical details will be involved.

4.1.1 Best-fitting

The scaling relations are assumed to take a simple power-law form

$$O \propto M_{\Delta}^{\beta}, \tag{4.1}$$

where O is the observable quantity (such as $L_{\rm bol}$,$L_{outofcore}$,$T_{\rm m}$,etc), M_{Δ} is the mass of the cluster and β is the power law index. This can be rewritten as

$$O = \alpha(M/M_{\rm pivot})_{\Delta}^{\beta} \tag{4.2}$$

where $M_{\rm pivot}$ is a pivot mass, the pivot mass is chosen to be the median of all the selected cluster masses, see section 3.10.1. Having a pivot point in the middle of the data minimises the co-variance between the parameters α and β.

Once the masses had been normalised in this way, the data were then fitted with a line of best fit

$$\log_e(O) = \log_e(\alpha) + \beta\ log_e(X), \tag{4.3}$$

where $X = M/M_{\rm pivot}$, α is the normalisation and β is the slope. The best fit lines where plotted in the code, using a IDL's LINFIT function.. LINFIT uses linear model to fit data, this is done by minimising the least-square error statistic. This is how the data in section 4.2 were calculated. The next part of the code is the generation of the scatter data.

4.1.2 Estimating the scatter

The scatter was obtained by first taking the least squares fit and calculating the residual for each data point.

$$\delta \log_e Y = \log_e[Y_i(X_i)] - \log_e[Y_{bf}(X_i)] \tag{4.4}$$

where $Y_i(X_i)$ is the value of each data and $Y_{bf}(X_i)$ is the best fit value for the same (X_i). A histogram is then constructed $\delta \log_e Y$, with 50 bins. A Gaussian function

is then fitted to the histogram, the Gaussian form being,

$$f(\delta \log_e Y) = A \exp -((\delta \log_e Y)^2/2\sigma^2) \tag{4.5}$$

where σ provides an estimate of the intrinsic scatter and A is the normalisation of the Gaussian. The next step in the code is calculation of the errors for each parameter.

4.1.3 Fit parameters errors

To account for statistical errors in the simulated data, the bootstrap method is used. The bootstrap method works as follows:

1. Create a new sample of data, sample i, by randomly picking out the same number of clusters ($N_{\rm cls}$) from the original sample. For bootstrapping it is important to note that duplication can and will occur.

2. Perform the fitting as before to get values for α, β and σ, for each scaling relation.

3. Repeat 1 and 2 many times to make a list of the fit parameters.

4. Assume that this list of fit parameters, comprised of many independent realisations of the same experiment, then find an acceptable number of realisations to perform.

5. This is done by comparing the mean value of the list of fit parameters to the true value of the parameter. The bootstrapped data will tend to the actual value after a certain number of realisations and that is the ideal number, X, of realisations to perform.

6. It is then possible to calculate the mean and standard deviation, or error, of the list of fit parameters. The standard deviation is taken as the error.

The errors of α, β, and σ are labelled as σ_α,σ_β and σ_σ respectively. Now the results from redshift zero can be analysed.

4.2 Results at redshift zero

This section shows the scaling relations at redshift zero, taken from the NMGS, using the method described in the section 4.1 to obtain the fit parameters. The catalogues chosen from the NMGS are the B ($\Delta = 200$) and C ($\Delta = 500$) catalogues the other catalogues are available in Appendix A.1, which are chosen to allow for a more accurate comparison to observations and the self-similar predictions.

4.2.1 Density contrasts

In tables 4.1 and 4.2, the fit parameters for the scaling relations from the two catalogues B and C are shown with their associated errors. The B catalogue contains more clusters and, therefore, the tables show that the errors in B are lower than that of C. This is another reason not to use the catalogues with larger Δ, because the errors increase with lower cluster count.

Scaling relation	$\log_e(\alpha)$	β	σ
$L_{\rm bol}$	-0.81 ± 0.01	1.60 ± 0.02	0.28 ± 0.01
$L_{\rm boloutcore}$	-0.75± 0.03	1.58 ± 0.01	0.18 ± 0.01
$T_{\rm m}$	0.82 ± 0.009	0.58 ± 0.004	0.06 ± 0.002
$T_{\rm sl}$	0.87 ± 0.009	0.56 ± 0.008	0.14 ± 0.004
$T_{\rm sloutcore}$	0.79 ± 0.010	0.57 ± 0.007	0.11 ± 0.003
$M_{\rm gas}$	30.8 ± 0.017	1.13 ± 0.005	0.06 ± 0.002
$Y_{\rm X}$	-12.1 ± 0.028	1.69 ± 0.010	0.16 ± 0.004
$Y_{\rm SZ}$	-12.1 ± 0.003	1.70 ± 0.006	0.10 ± 0.003
Q	0.97 ± 0.01	0.06 ± 0.02	0.19 ± 0.01

Table 4.1: Fit parameters for the B catalogue, with 939 clusters and 10,000 realisations used with a pivot mass of 1.96×10^{14} solar masses. Relations are in the form of $O \propto M_{200}$.

The results can now be compared to the self-similar predictions for β, see table 3.2, and the other fit parameters can also be discussed. We discuss each relation in turn:

- The $L_{\rm bol} - M_{\Delta}$ relation for B has a β of 1.6 disagreeing with the self-similar prediction of 4/3; this is the same result as for C which has only a slightly lower

Scaling relation	$\log_e(\alpha)$	β	σ
$L_{\rm bol}$	-0.13 ± 0.010	1.52 ± 0.023	0.23 ± 0.010
$L_{\rm boloutcore}$	-0.34 ± 0.007	1.54 ± 0.019	0.18 ± 0.008
$T_{\rm m}$	1.07 ± 0.002	0.58 ± 0.005	0.07 ± 0.002
$T_{\rm sl}$	1.08 ± 0.003	0.54 ± 0.010	0.10 ± 0.004
$T_{\rm sloutcore}$	1.04 ± 0.003	0.55 ± 0.008	0.08 ± 0.004
$M_{\rm gas}$	30.5 ± 0.002	1.13 ± 0.005	0.06 ± 0.002
$Y_{\rm X}$	-12.2 ± 0.004	1.67 ± 0.012	0.12 ± 0.005
$Y_{\rm SZ}$	-12.2 ± 0.003	1.70 ± 0.007	0.08 ± 0.003
Q	0.58 ± 0.007	0.09 ± 0.017	0.17 ± 0.008

Table 4.2: Fit parameters for the C catalogue, with 684 clusters and 10,000 realisations used with a pivot mass of 1.53×10^{14} solar masses. Relations are in the form of $O \propto M_{500}$.

β of 1.5. This suggests that the lower mass clusters have a lower luminosity than expected as required to match observational data.

- When subtracting the core luminosity from the total luminosity of the cluster, $L_{\rm boloutcore} - M_\Delta$, it is found that in catalogue B, β is only slightly lower than the original $L_{\rm bol}$ result. We also find a lower scatter in the $L_{\rm boloutcore}$ result. Since β does not change much, this suggests that most of the non-similar behaviour is not due to the core.

- For temperature weighted mass, $T_{\rm m}$, both catalogues have a very similar β value, which are found to be lower than the self-similar result. This suggests that the temperature is higher in lower mass clusters than the self-similar model predicts, again required by observations.

- For $T_{\rm sl} - M_\Delta$ we find a lower β than the $T_{\rm m}$ for both catalogues, however, C has a lower β than B, but this is not particularly significant. When both catalogue's β are compared to the self-similar model, the same result as $T_{\rm m}$ is found. The lower value of β would suggest that the temperature is directly affected by the feedback in the NMGS. Furthermore the fact that $T_{\rm sl}$ and $T_{\rm m}$ are very similar suggests that the clumping factor is not a function of mass. A difference between $T_{\rm sl}$ and $T_{\rm m}$ is found in the scatter, σ, with $T_{\rm sl}$ being noisier than $T_{\rm m}$.

- $T_{\rm sloutcore} - M_{\Delta}$ is very similar to the $T_{\rm sl} - M_{\Delta}$ result with slightly less scatter, as with $L_{\rm boloutcore}$ result.

- Although $M_{\rm gas} - M_{\Delta}$ is not directly observable, it can nevertheless be deduced from the soft X-ray surface brightness profile, it still exhibits some shift away from the self-similar prediction of $\beta = 1$. Both catalogues agree on the value of β being slightly larger than unity. This is due to feedback heating the gas and expanding it, leading to lower gas fractions in lower mass clusters (where feedback is more effective).

- For $Y_{\rm X} - M_{\Delta}$ from the C catalogue, β agrees with the self-similar predictions, however, the β from the B catalogue is slightly larger. This suggests that feedback heats the gas (increasing T) and decreasing $M_{\rm gas}$. The two effects partly cancel each other out. We find the $Y_{\rm SZ} - M_{\Delta}$ values very similar.

- For $Q - M_{\Delta}$, while not an observable, does depend on mass, contrary to the self-similar model, suggesting that cluster's density structure is mass dependent.

In conclusion, the main result of this section is that most of the scaling relations tend to deviate from the self-similar model. This is akin to observational data in the section 2. A breakdown of the scaling relations is now performed to see if any of the deviations in properties are correlated with one another.

4.3 Correlation analysis

Correlation analysis is used to compare two scaling relations to one another, allowing for analysis on the interdependence of the scaling relations. Another good reason for using correlation analysis is that it allows for a direct comparison with [Stanek et al., 2010], who presented the covariance matrices for the GO and PC simulations. Here, the details of the correlation analysis is presented alongside the results from the NMGS, before comparing with [Stanek et al., 2010].

4.3.1 Pearson's correlation coefficient

For the correlation analysis we calculate r_{ij}, the Pearson product-moment correlation coefficient (PPMCC):

$$r_{ij} = \frac{\bar{Z}_{ij}}{\sigma_i \sigma_j}, \tag{4.6}$$

where $\bar{Z}_{ij}$ is,

$$\bar{Z}_{ij} = \langle \delta i \delta j \rangle - \langle \delta i \rangle \langle \delta j \rangle \tag{4.7}$$

and

$$\sigma_i^2 = \langle \delta i^2 \rangle - \langle \delta i \rangle^2 \tag{4.8}$$

where δi and δj are $\delta \log_e$ values for the two scaling relations, and the σ values are the Gaussian fits for the scatter. The return from the PPMCC ranges from 1, which means the residuals δi and δj are well correlated, to -1 (anti-correlated) and a value of zero signifies being no correlation at all.

4.3.2 Results

Scaling relation	$L_{\rm bol}$	$L_{\rm boloutcore}$	$T_{\rm m}$	$T_{\rm sl}$	$T_{\rm sloutofcore}$	$M_{\rm gas}$	$Y_{\rm X}$	$Y_{\rm SZ}$	Q
$L_{\rm bol}$	...	0.90	0.46	0.76	0.68	0.63	0.89	0.75	0.94
$L_{\rm boloutcore}$	0.90	...	0.40	0.58	0.59	0.66	0.75	0.73	0.81
$T_{\rm m}$	0.46	0.40	...	0.82	0.87	0.06	0.71	0.73	0.48
$T_{\rm sl}$	0.76	0.58	0.82	...	0.96	0.22	0.92	0.72	0.78
$T_{\rm sloutcore}$	0.68	0.59	0.87	0.96	...	0.17	0.87	0.72	0.70
$M_{\rm gas}$	0.63	0.66	0.06	0.22	0.17	...	0.57	0.72	0.33
$Y_{\rm X}$	0.89	0.75	0.71	0.92	0.87	0.57	...	0.88	0.78
$Y_{\rm SZ}$	0.75	0.73	0.73	0.72	0.72	0.72	0.88	...	0.56
Q	0.94	0.81	0.48	0.78	0.70	0.33	0.78	0.56	...

Table 4.3: Here the scaling relations are compared with one another, via the PPMCC. This uses redshift zero data taken from the C catalogue with a cluster count of 684. The C catalogue was used because it is the same catalogue [Stanek et al., 2010] used for their simulated results.

Here, in table 4.3, it can be seen that the relations with obvious dependence like Q and $L_{\rm bol}$ (see section 2.2.3) have high values for PPMCC, whereas the scatter in $M_{\rm gas}$ and $T_{\rm sloutcore}$ are almost uncorrelated. Scaling relations with high interdependence cause deviation from self-similar in one to appear in the other, even ones which are

structure relations like Q.

This data seems to agree reasonably well with the results from the [Stanek et al., 2010] paper, although we tend to find stronger correlation with Q. In that paper the preheating model (PC) was being used, which simulates the gas physics with additional energy at high redshift. This model compares well to our feedback only simulation, NMGS. However, the [Stanek et al., 2010] paper also includes a GO model, MS, which is not as similar to the data. This is due to the additional gas physics present in our model.

The extra gas physics are the feedback from AGN, supernovae feedback and metals present in the ICM. A way to test the data gathered here is to compare the scaling relations to observational data.

4.4 Observational data comparisons

This should provide evidence that the data gathered from NMGS is an accurate representation of clusters. This is the only method of testing our relations left, since both the observational data and the scaling relation data from the NMGS seem to deviate from the self-similar model.

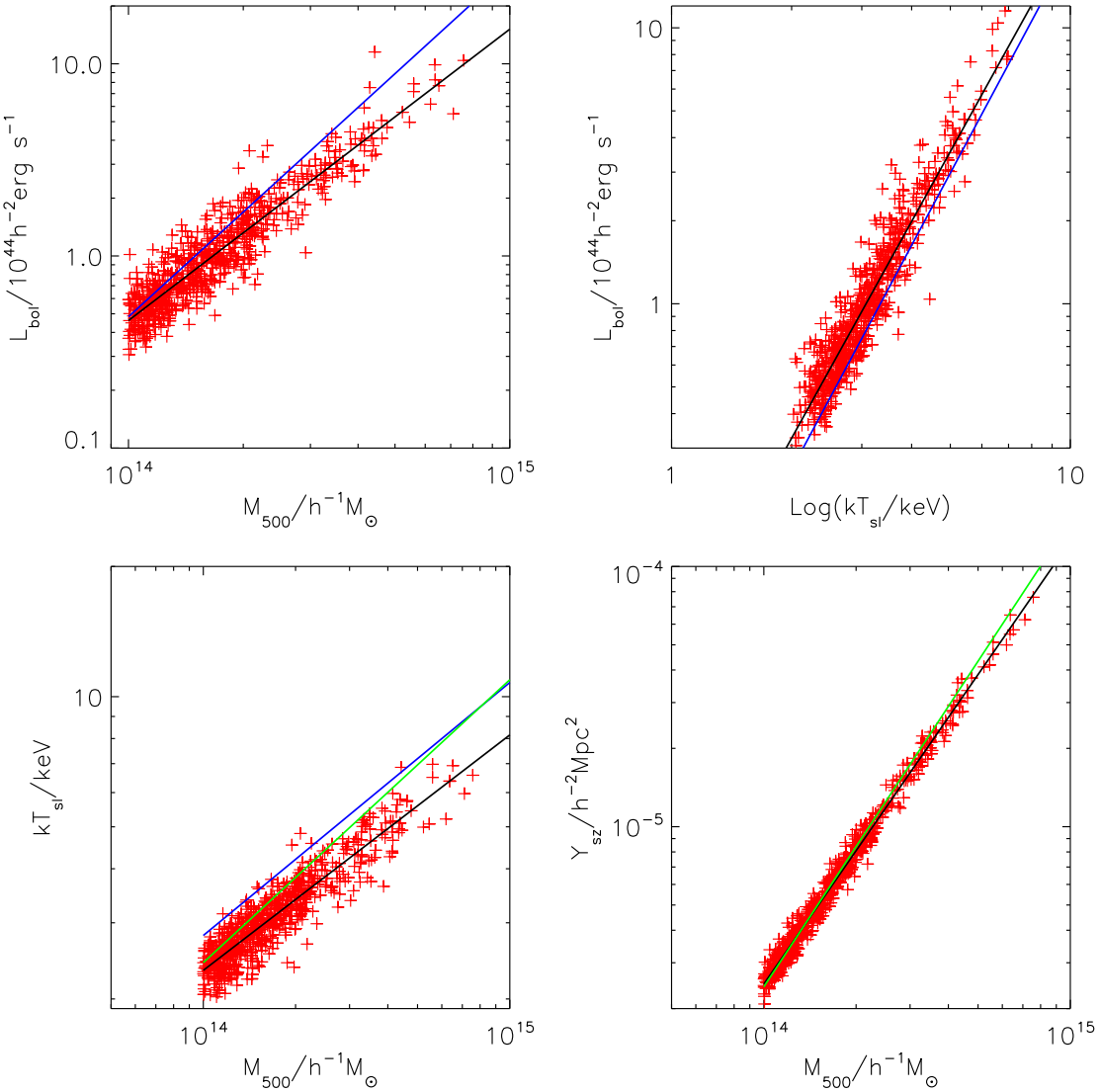

Figure 4.1: In this figure clusters are plotted as red plus signs, the line of best fit, see section 4.1, is plotted in black and the observational data is plotted in blue and green respectively. The data was taken from the 500 Mpc/h box and is the C catalogue. The top left panel shows $L_{\rm bol} - M_{500}$ relation, the blue line is the observational result from [Pratt et al., 2009]. The top right panel is $L_{\rm bol} - T_{\rm sl}$ relation, with the blue line from [Pratt et al., 2009]. The bottom left panel shows the $T_{\rm sl} - M_{500}$ relation, with the blue line from [Arnaud et al., 2005] and the green line from [Vikhlinin et al., 2009]. The bottom right panel shows the $Y_{\rm SZ} - M_{500}$ relation, with the green line taken from [Planck Collaboration et al., 2011].

In figure 4.1 the scaling relations chosen are $L_{\rm bol} - M_{500}$, $L_{\rm bol} - T_{\rm sl}$, $T_{\rm sl} - M_{500}$ and $Y_{\rm SZ} - M_{500}$. These were chosen due to the ability to compare them to observational data. One issue with observational results is that they use different units and pivot points, which must be converted in order to compare them with our results. So in the interest of time, only the C catalogue was used. We discuss the results listed

here:

- The top left panel of figure 4.1 is the $L_{\rm bol} - M_{500}$ relation, with results from the [Pratt et al., 2009] paper plotted as the blue line. The [Pratt et al., 2009] data agree well with our data for low mass clusters, however, not as well for high mass clusters.

- The $L_{\rm bol} - T_{\rm sl}$ relation is in the top right panel, with the result from the blue line again from [Pratt et al., 2009]. The [Pratt et al., 2009] result shows a slightly higher temperature than our results.

- The bottom left panel contains the $T_{\rm sl} - M_{500}$ relation, with the blue line from [Arnaud et al., 2005] and the green line from [Vikhlinin et al., 2009]. The [Vikhlinin et al., 2009] results agree well at lower mass but deviates at higher masses. The result from [Arnaud et al., 2005] shows that the clusters they selected have a higher temperature but a similar β to our data, which is encouraging.

- We find for the bottom right panel, the $Y_{\rm SZ} - M_{500}$ relation, with the green line taken from the [Planck Collaboration et al., 2011] paper. We find that our result is in agreement with a recent instrument.

Our data seem to not agree well with the observational results, particularly the $L_{\rm bol} - T_{\rm sl}$ relation from [Pratt et al., 2009]. The results are similar to FO data at redshift zero from [Short et al., 2010]. They find that the scaling relations match the ones taken from clusters in the REXCESS sample, once they accounted the observed lower cluster mass bias (10-20%). This is caused by the assumption that the clusters are in hydrostatic equilibrium.

The extra non-gravitational heating found in the NMGS is able to break self-similarity. In order to further analyse the scaling relations we have applied the same methodology with a few tweaks to find results at higher redshift.

Chapter 5

Evolution of the scaling relations with redshift

This chapter examines the scaling relations at different redshifts. The individual results for the scaling relations with redshifts are shown in groups, so relations that are similar can be compared with one another. A discussion of the results finishes this chapter. However, firstly the self-similar dependence is examined, so that the results are presented relative to these predictions.

5.1 Self-similar prediction

The self-similar model predicts the slope to remain constant and only the normalisation to vary with redshift. Non-self-similar behaviour could result in both a varying slope and a different redshift dependence for the normalisation. To test the scaling relations against the self-similar, the scaling relations are normalised,

$$\frac{Y}{E(z)^d} \propto X^\beta \tag{5.1}$$

where Y is the observable of the clusters, d is the power-law index of the $E(z)$ dependence and X is mass (or temperature). The values of d of each scaling relation are shown in table 5.1.

Scaling relation	d
$L_{\rm bol}$ vs M_Δ	7/3
$L_{\rm boloutofcore}$ vs M_Δ	7/3
$T_{\rm m}$ vs M_Δ	2/3
$T_{\rm sl}$ vs M_Δ	2/3
$T_{\rm sloutofcore}$ vs M_Δ	2/3
$M_{\rm gas}$ vs M_Δ	0
$Y_{\rm X}$ vs M_Δ	2/3
$Y_{\rm SZ}$ vs M_Δ	2/3
Q vs M_Δ	0
$L_{\rm bol}$ vs $T_{\rm sl}$	1
$L_{\rm bol}$ vs $T_{\rm sloutofcore}$	1
$L_{\rm boloutofcore}$ vs $T_{\rm sloutofcore}$	1

Table 5.1: The scaling relations dependence on the power-law index of the $E(z)$

In the next sections the scaling relations will be investigated at different redshifts, these results show the relations after correction for the expected self similar evolution. The results have a pivot mass of 1.96×10^{14} for the B catalogue and 1.53×10^{14} for the C catalogue.

5.2 Results

The redshift range is from 0 to 1, with 24 separate redshifts in total. The same methodology is used for the redshift zero data (see section 4 for the fitting method). The maximum redshift is justified by the limited cluster count, which drops from around 10^3 clusters, in the B catalogue at redshift 0, to $\simeq 64$, in the C catalogue at redshift 1. Any statistical analysis, such as bootstrap, is unlikely to produce reliable results when the cluster counts are too low. Similar scaling relations are grouped together so that related quantities can be readily compared.

5.2.1 Luminosity-Mass Relations

This section presents the relations which relate luminosity and mass; $L_{\rm bol} - M_\Delta$, $L_{\rm boloutofcore} - M_\Delta$ and $Q - M_\Delta$. Figure 5.1 shows the best fit lines for each relation at three different redshifts, based on catalogue B. The relations cover a smaller mass range as redshift increases, because it takes time for clusters to accrue mass, so

there are fewer high mass clusters at high redshift. All the relations tend to evolve even after self-similar evolution has been removed, with $Q - M_\Delta$ evolving the most. Clearly the luminosity increases with redshift, this is related to AGN feedback, since feedback increases the temperature of the ICM and makes the ICM more diffuse with decreasing redshift. $Q - M_\Delta$ evolves which suggests, as with the redshift zero results, that it is dependent on mass. This is different to [Stanek et al., 2010] who find a weaker correlation of $Q - M_\Delta$ then this result.

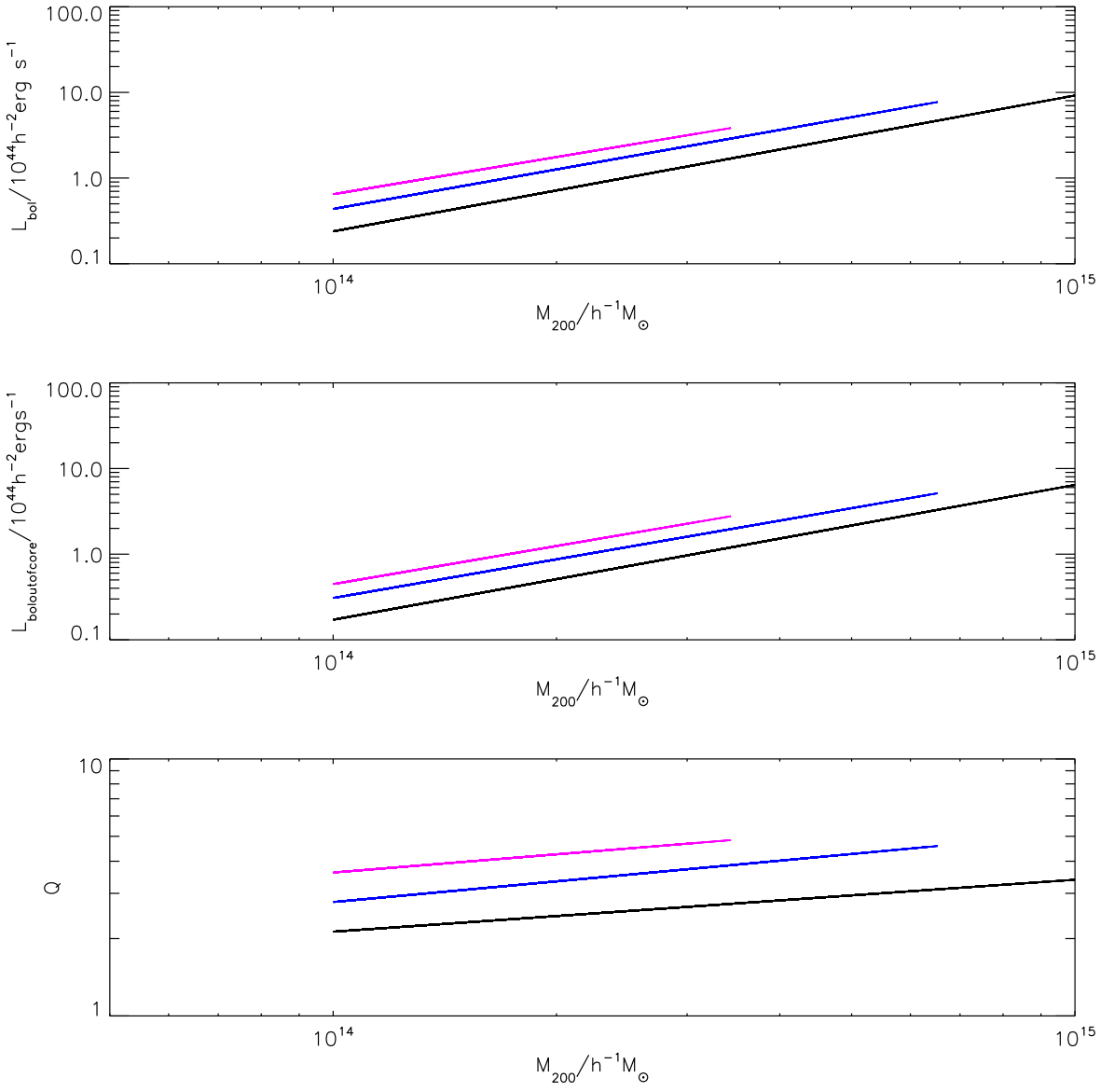

Figure 5.1: This figure shows the best fit line at redshift 0, 0.5, and 1 for the scaling relations that relate temperature to mass, $L_{\rm bol} - M_\Delta$, $L_{\rm boloutcore} - M_\Delta$ and $Q - M_\Delta$ respectively. The black line represents the result at redshift zero, the blue line redshift 1/2 and pink for redshift one.

The following graphs are the result of examining whether the fit parameters of the scaling relations discussed previously evolve over redshift.

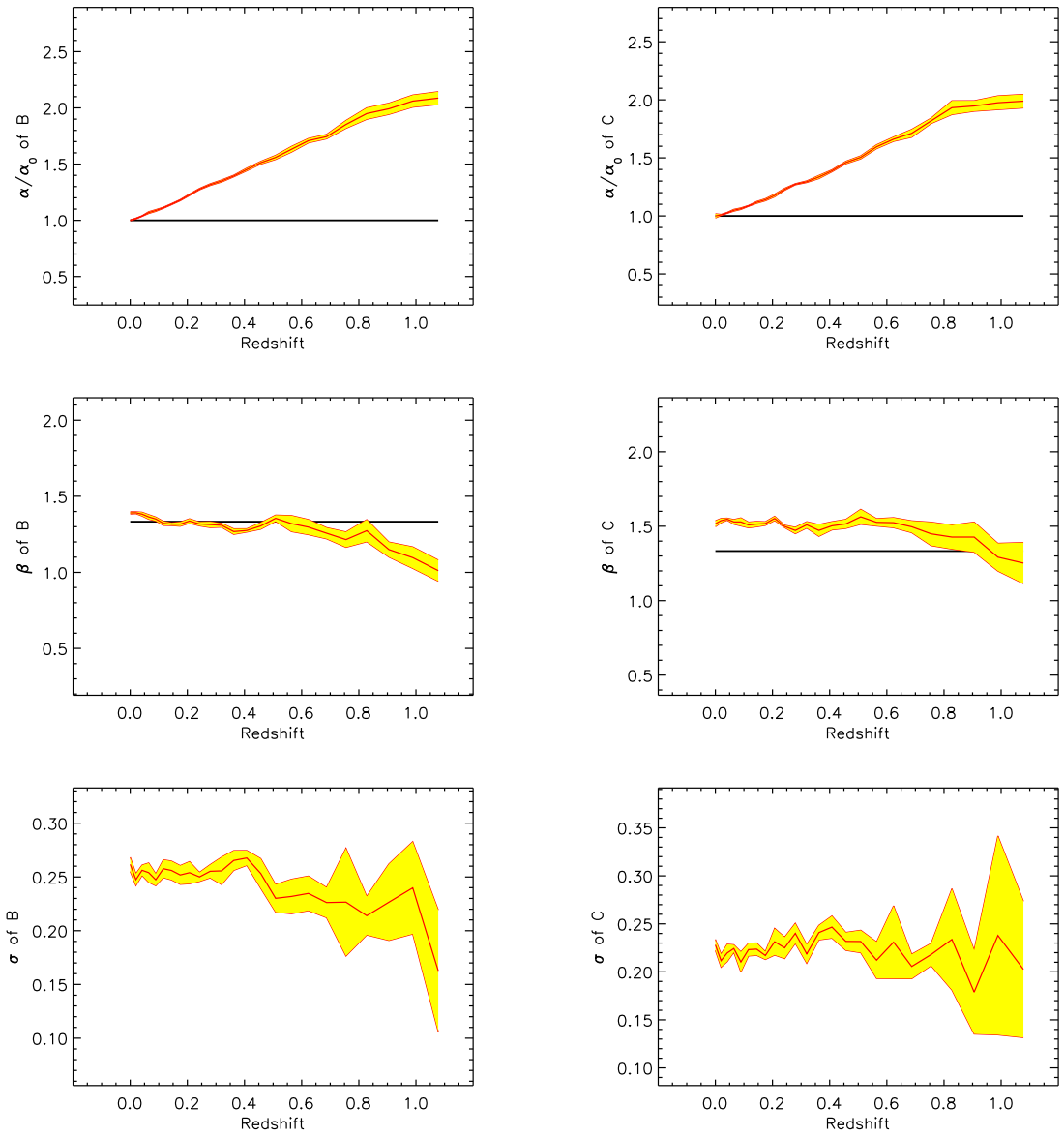

Figure 5.2: This figure shows the fit parameters for $L_{\rm bol}/E(z)^{7/3}$ vs M_Δ at 24 different redshifts on the x-axis, from two catalogues B ($L_{\rm bol}/E(z)^{7/3}$ vs M_{200}) and C ($L_{\rm bol}/E(z)^{7/3}$ vs M_{500}) in the left and right columns respectively. The intercept, α, is shown in the top two graphs, where the y-axis is α normalised by the result at redshift zero and the self-similar model prediction is represented by the black line. The slopes, β, are plotted in the middle two graphs, with the self-similar model prediction represented by the black line. The bottom graphs are the scatter, σ, at each redshift. All subsequent figures in this section follow the same layout.

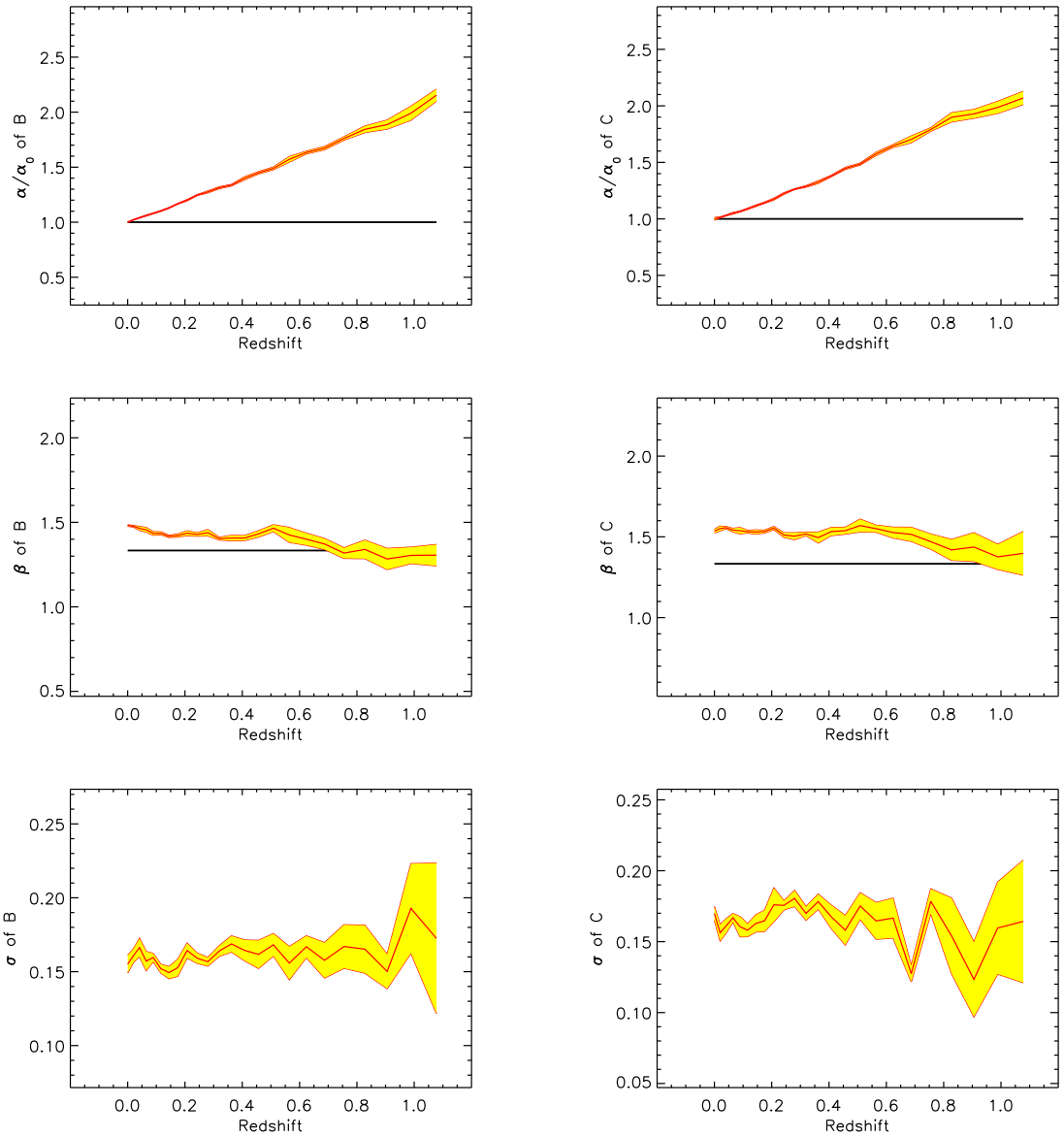

Figure 5.3: This figure shows the fit parameters for $L_{\rm boloutcore}/E(z)^{7/3}$ vs M_{Δ} at 24 different redshifts from two catalogues B ($L_{\rm boloutcore}/E(z)^{7/3}$ vs M_{200}) and C ($L_{\rm boloutcore}/E(z)^{7/3}$ vs M_{500}) in the left and right columns respectively.

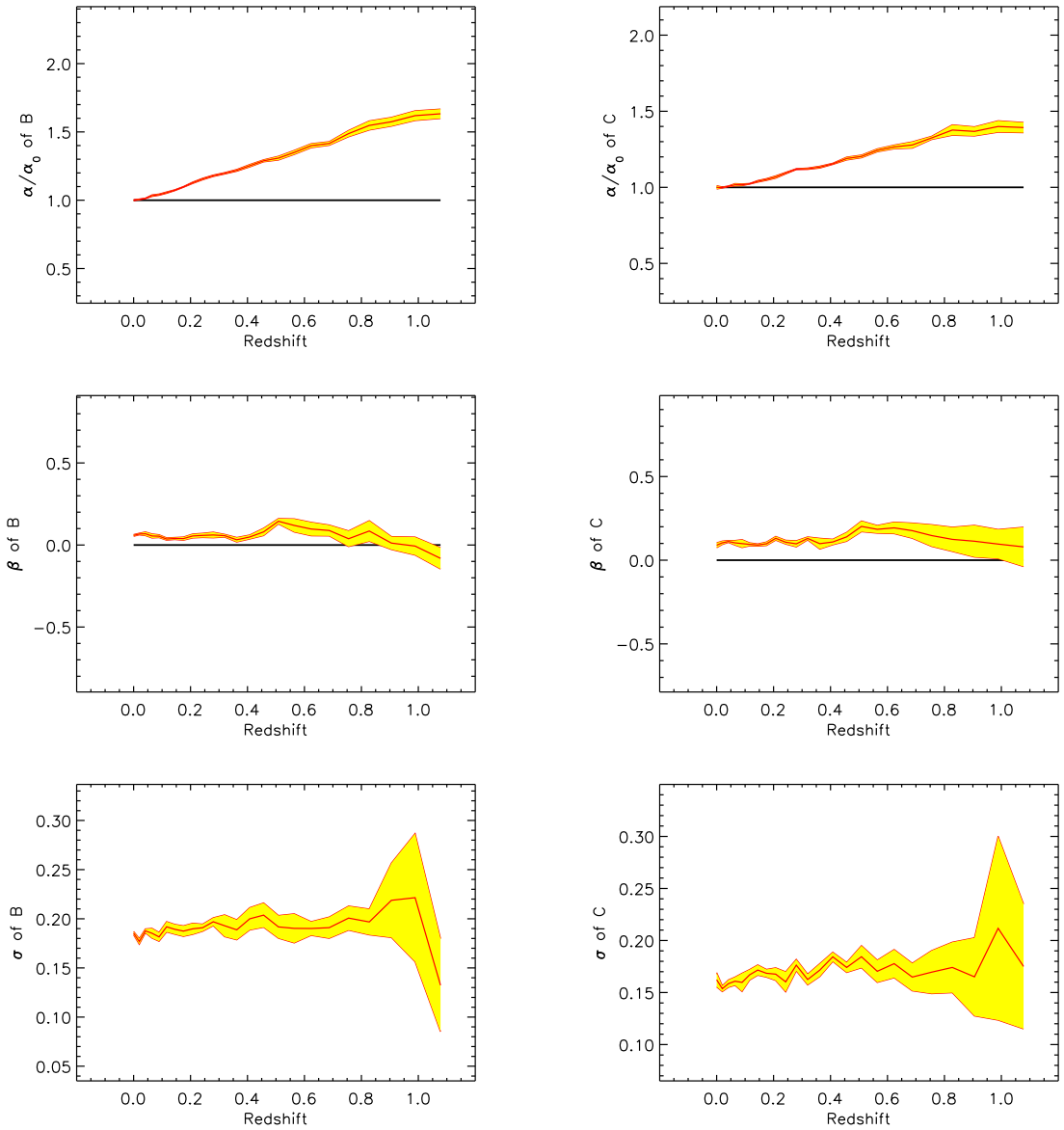

Figure 5.4: This figure shows the fit parameters for Q vs M_Δ at 24 different redshifts, from two catalogues B (Q vs M_{200}) and C (Q vs M_{500}) in the left and right columns respectively.

Table 5.2 serves as a summary for graphs 5.2, 5.3 and 5.4. We find that the normalisation, α, for all the relations from both catalogues show a similar evolution, with the $Q - M_\Delta$ relation being slightly lower. This disagrees with the self-similar predictions. The $Q - M_\Delta$ relation also differs from the other luminosity relations for it has a flat scatter, which implies that the number of the clusters does not effect the scatter of the $Q - M_\Delta$ relation. When examining the slopes, β, of the luminosity relations it is found that they tend to the self-similar result as redshift increases. This is for the same reason as previously mentioned, it is caused by the

AGN feedback.

Scaling relation	Redshift	$(\alpha/\alpha_0)_{\rm B}$	$(\alpha/\alpha_0)_{\rm C}$	$\beta_{\rm B}$	$\beta_{\rm C}$	$\sigma_{\rm B}$	$\sigma_{\rm C}$
$L_{\rm bol}$ vs M_Δ	0.0	1.00	1.00	1.39	1.52	0.26	0.23
$L_{\rm bol}$ vs M_Δ	0.5	1.56	1.50	1.36	1.56	0.23	0.23
$L_{\rm bol}$ vs M_Δ	1.0	2.09	1.99	1.01	1.25	0.16	0.20
$L_{\rm boloutofcore}$ vs M_Δ	0.0	1.00	1.00	1.48	1.54	0.16	0.17
$L_{\rm boloutofcore}$ vs M_Δ	0.5	1.49	1.48	1.47	1.57	0.17	0.18
$L_{\rm boloutofcore}$ vs M_Δ	1.0	2.15	2.07	1.31	1.40	0.17	0.16
Q vs M_Δ	0.0	1.00	1.00	0.06	0.09	0.19	0.16
Q vs M_Δ	0.5	1.31	1.20	0.14	0.20	0.19	0.18
Q vs M_Δ	1.0	1.63	1.39	-0.08	0.08	0.13	0.18

Table 5.2: Fit parameters for the scaling relations which relate luminosity to mass, where $(\alpha/\alpha_0)_{\rm B}$ is α normalised by α at redshift zero, α_0, for catalogue B and $(\alpha/\alpha_0)_{\rm C}$ is α normalised by α at redshift zero for catalogue C.

5.2.2 Temperature-Mass Relations

This section analyses the relations which relate temperature to mass: $T_{\rm m} - M_\Delta$, $T_{\rm sl} - M_\Delta$ and $T_{\rm sloutofcore} - M_\Delta$. Figure 5.5 shows the lines of best fit for those relations at three different redshifts. Very little evolution is found in the $T_{\rm sl} - M_\Delta$ and $T_{\rm sloutofcore} - M_\Delta$ relations, however,$T_{\rm m} - M_\Delta$ shows some slight evolution. Because self-similar evolution has been removed from these lines of best fit, this must be caused feedback from AGN.

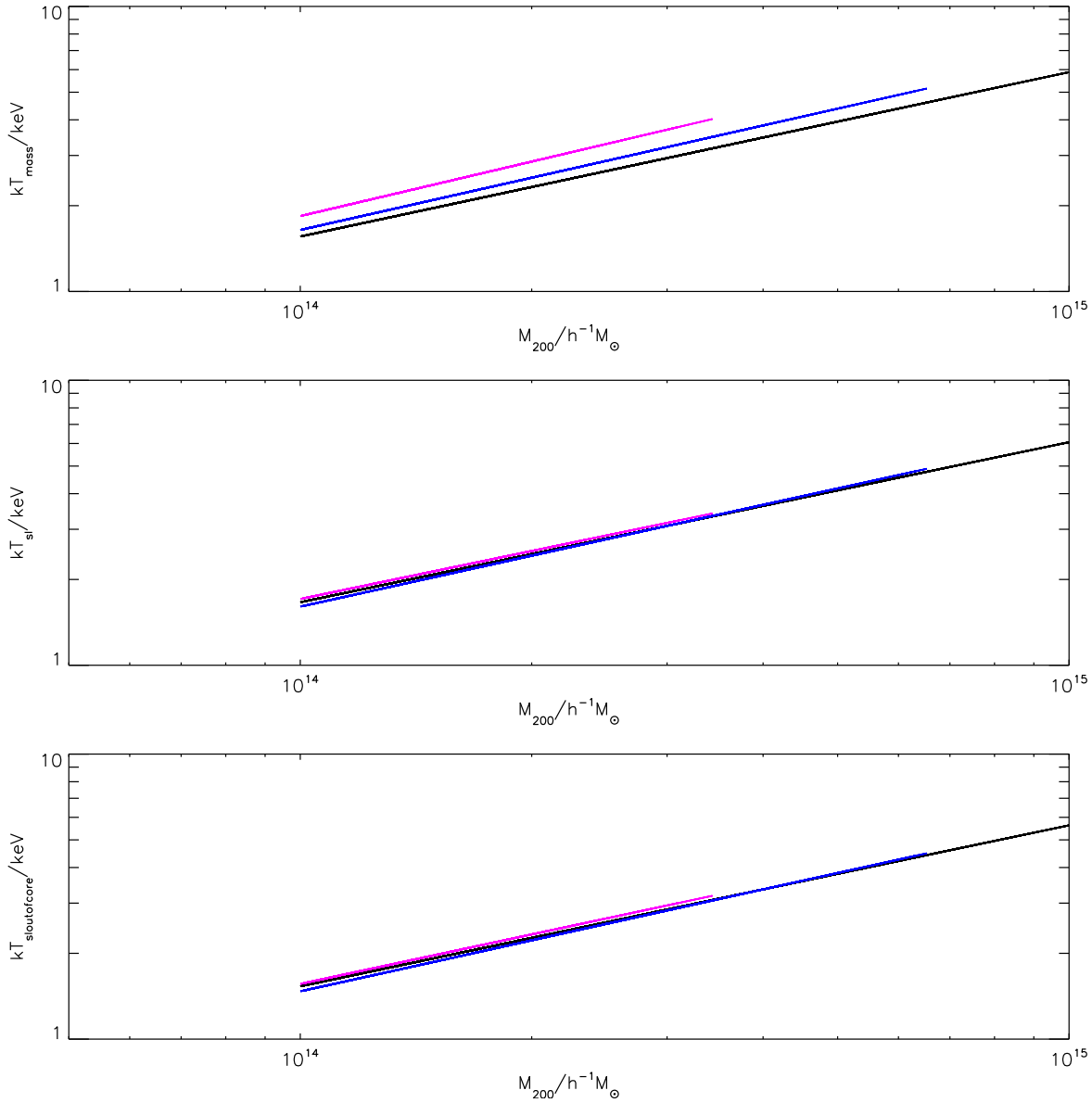

Figure 5.5: This figure shows the best fit line at redshift 0, 0.5, and 1 for the scaling relations that relate temperature to mass, $T_{\rm m} - M_{\Delta}$, $T_{\rm sl} - M_{\Delta}$ and $T_{\rm sloutofcore} - M_{\Delta}$ respectively. The black line represents the result at redshift zero, the blue line redshift 1/2 and pink for redshift one.

These next graphs are the product of examining whether the fit parameters of the scaling relations, which relate temperature to mass, evolve over redshift.

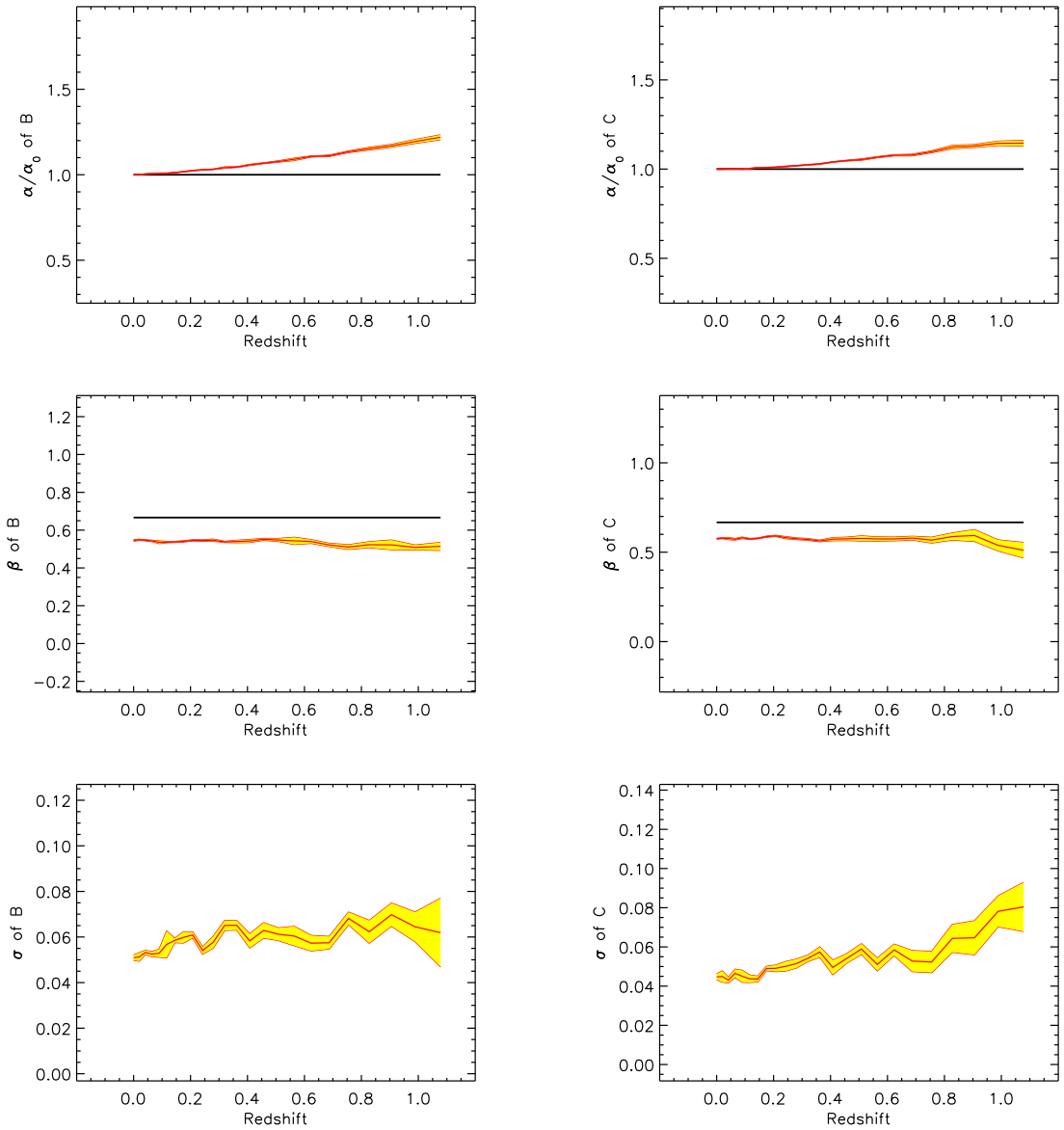

Figure 5.6: This figure shows the fit parameters for $T_{\rm m}/E(z)^{2/3}$ vs M_{Δ} at 24 different redshifts on the x-axis, from two catalogues B ($T_{\rm m}/E(z)^{2/3}$ vs M_{200}) and C ($T_{\rm m}/E(z)^{2/3}$ vs M_{500}) in the left and right columns respectively. The intercept, α, is shown in the top two graphs, where the y-axis is α normalised by the result at redshift zero and the self-similar model prediction is represented by the black line. The slopes, β, plotted in the middle two graphs, with the self-similar model prediction is represented by the black line. The bottom graphs are the scatter, σ, at each redshift. All subsequent figures in this section follow the same layout.

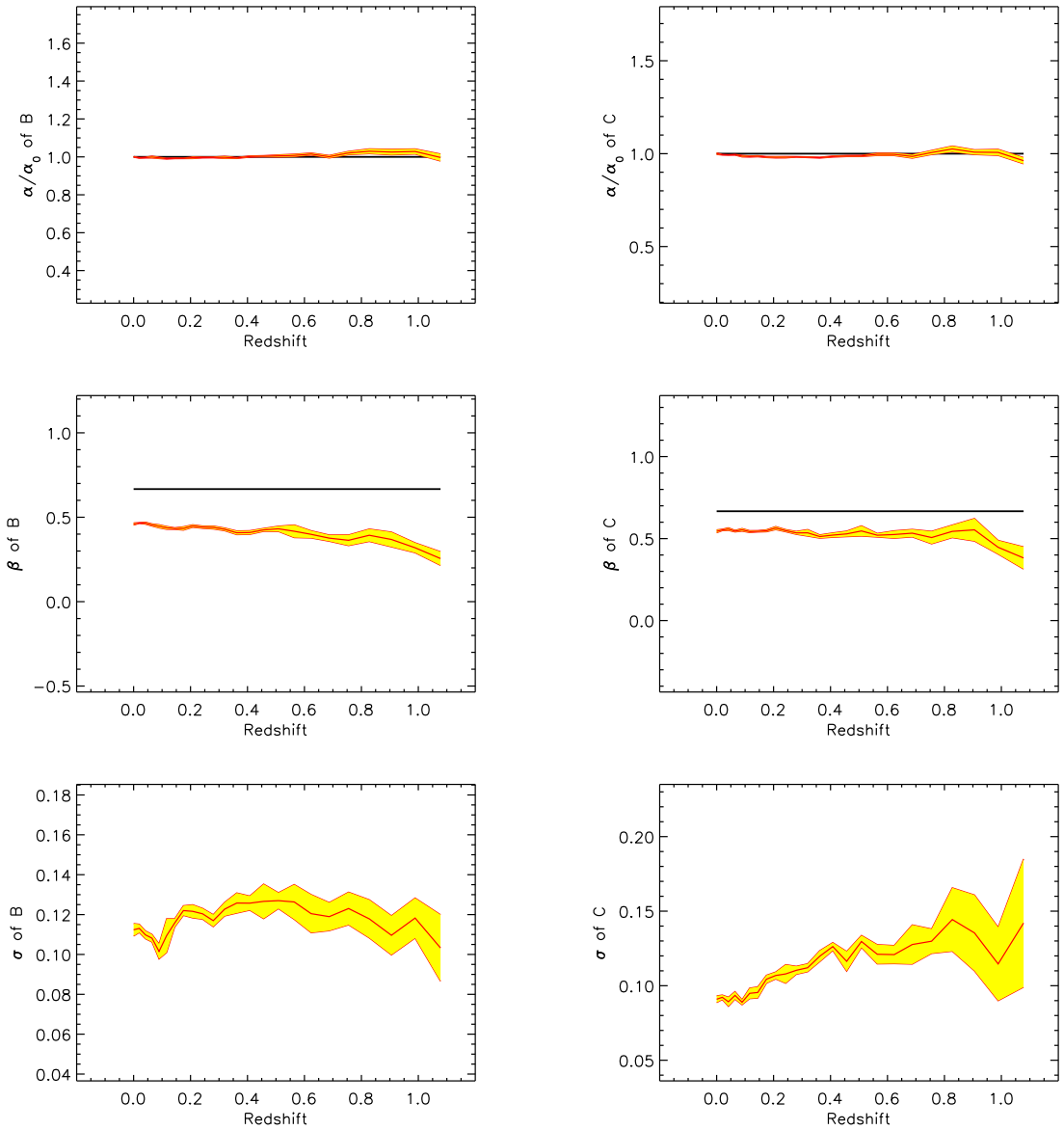

Figure 5.7: This figure shows the fit parameters for $T_{\rm sl}/E(z)^{2/3}$ vs M_Δ at 24 different redshifts from two catalogues B ($T_{\rm sl}/E(z)^{2/3}$ vs M_{200}) and C ($T_{\rm sl}/E(z)^{2/3}$ vs M_{500}) in the left and right columns respectively.

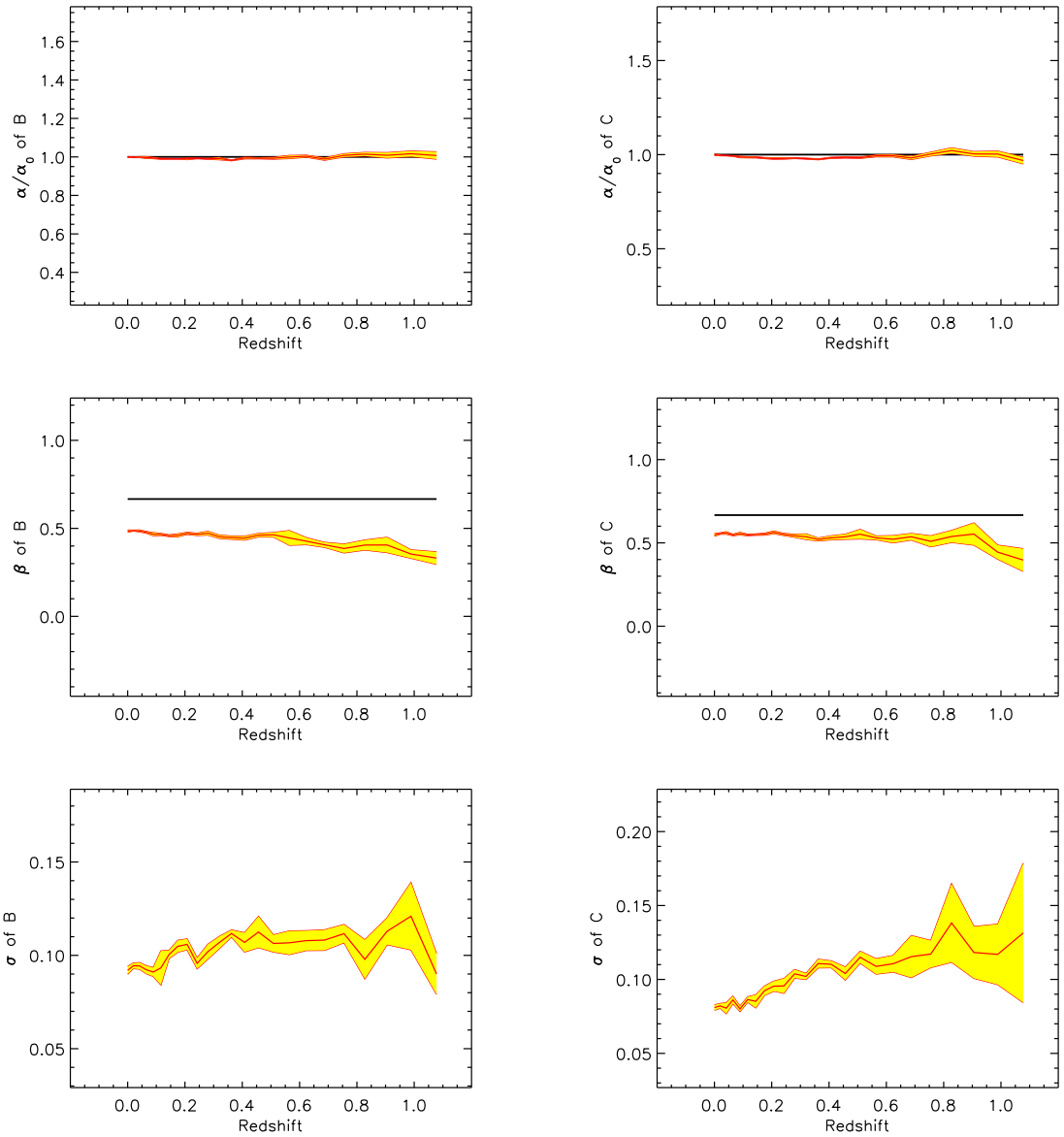

Figure 5.8: This figure shows the fit parameters for $T_{\rm sloutcore}/E(z)^{2/3}$ vs M_Δ at 24 different redshifts from two catalogues B ($T_{\rm sloutcore}/E(z)^{2/3}$ vs M_{200}) and C ($T_{\rm sloutcore}/E(z)^{2/3}$ vs M_{500}) in the left and right columns respectively.

Table 5.3 serves as a summary for graphs 5.6, 5.7 and 5.8. Again from the normalisation, α, it is seen that spectroscopic temperatures are flat and have no evolution, whereas the $T_{\rm m} - M_\Delta$ relation has some slight evolution from the self-similar prediction. AGN feedback must lower the mass of the cluster slightly to alter this relation. Furthermore, the $T_{\rm m} - M_\Delta$ has the lowest scatter, σ, of the relations.

We find very little evolution in the slopes, β, of any of the temperature mass relations, the relations tend to lie slightly below the self-similar prediction. Similar to the redshift zero results, we see that the C catalogue results are lower than B but

this is not particularly significant. The same result holds from redshift zero, with $T_{\rm m} - M_{\Delta}$ and $T_{\rm sl} - M_{\Delta}$ very similar, implying that the ICM is not very clumpy in this model even at high redshift.

Scaling relation	Redshift	$(\alpha/\alpha_0)_{\rm B}$	$(\alpha/\alpha_0)_{\rm C}$	$\beta_{\rm B}$	$\beta_{\rm C}$	$\sigma_{\rm B}$	$\sigma_{\rm C}$
$T_{\rm m}$ vs M_{Δ}	0.0	1.00	1.00	0.55	0.58	0.05	0.04
$T_{\rm m}$ vs M_{Δ}	0.5	1.08	1.05	0.55	0.58	0.06	0.06
$T_{\rm m}$ vs M_{Δ}	1.0	1.22	1.15	0.51	0.51	0.06	0.08
$T_{\rm sl}$ vs M_{Δ}	0.0	1.00	1.00	0.46	0.54	0.11	0.09
$T_{\rm sl}$ vs M_{Δ}	0.5	1.01	0.99	0.43	0.55	0.13	0.13
$T_{\rm sl}$ vs M_{Δ}	1.0	1.00	0.96	0.26	0.38	0.10	0.14
$T_{\rm sloutofcore}$ vs M_{Δ}	0.0	1.00	1.00	0.48	0.55	0.09	0.08
$T_{\rm sloutofcore}$ vs M_{Δ}	0.5	0.99	0.98	0.46	0.55	0.11	0.12
$T_{\rm sloutofcore}$ vs M_{Δ}	1.0	1.01	0.97	0.33	0.40	0.09	0.13

Table 5.3: Fit parameters for the scaling relations which relate temperature to mass, where $(\alpha/\alpha_0)_{\rm B}$ is α normalised by α at redshift zero, α_0, for catalogue B and $(\alpha/\alpha_0)_{\rm C}$ is α normalised by α at redshift zero for catalogue C.

5.2.3 $M_{\rm gas}$-Mass relation

Here the results for $M_{\rm gas} - M_{200}$ and $M_{\rm gas} - M_{500}$ are analysed. Figure 5.9 shows the lines of best fit for $M_{\rm gas} - M_{200}$ at three different redshifts. The results show a flat evolution of the $M_{\rm gas} - M_{200}$ relation, which is in good agreement with the self-similar prediction.

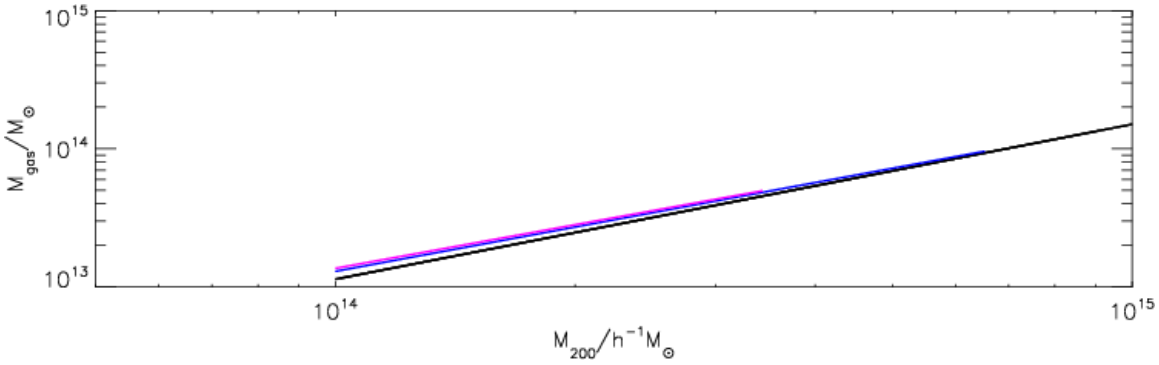

Figure 5.9: This figure shows the best fit line at redshift 0, 0.5, and 1 for the scaling relations that relate gas mass to mass, $M_{\rm gas} - M_{200}$. The black line represents the result at redshift zero, the blue line redshift 1/2 and pink for redshift one.

The following graph is the result of examining whether the fit parameters of the $M_{\rm gas} - M_{\Delta}$ relation evolves over redshift.

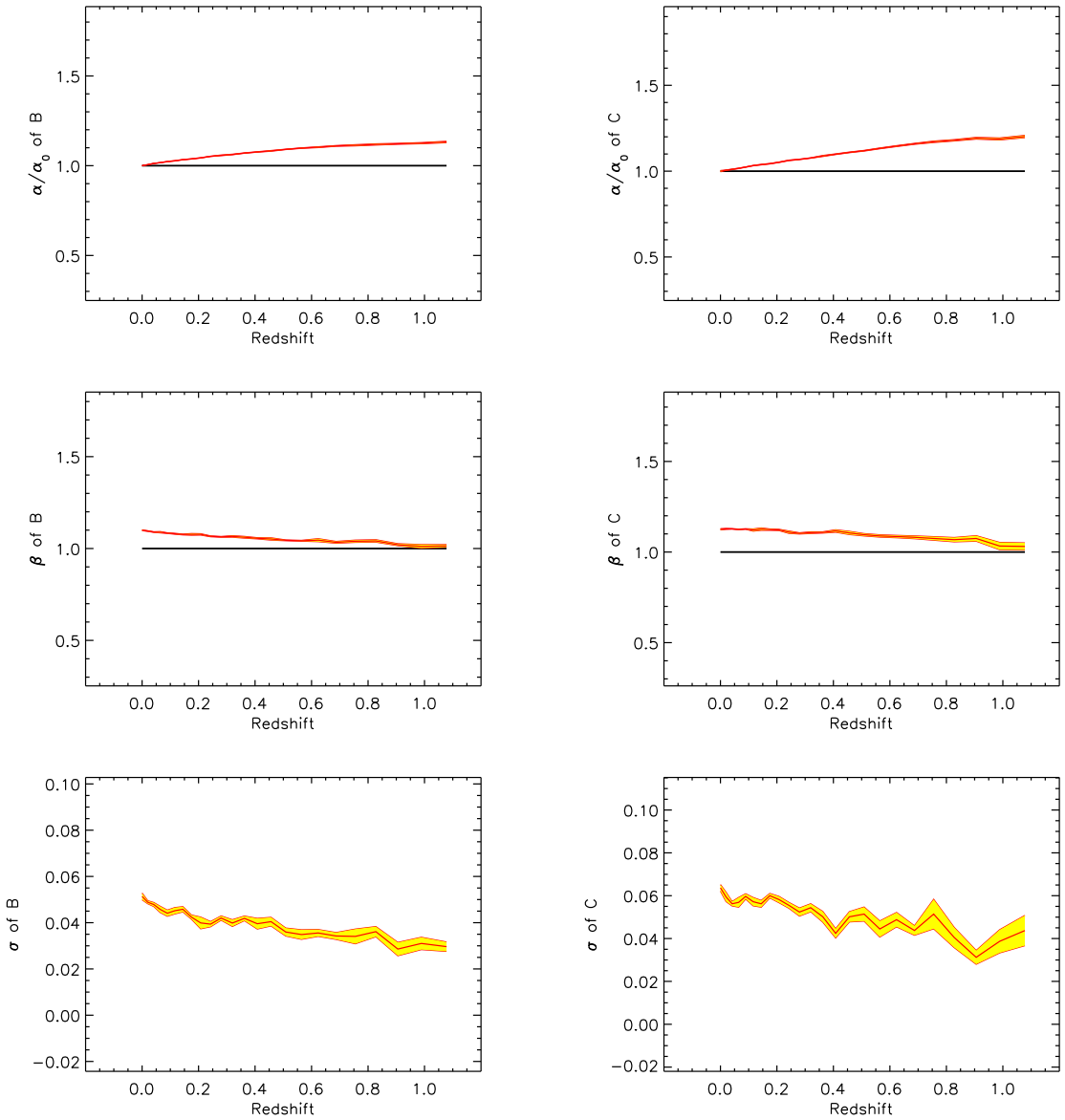

Figure 5.10: This figure shows the fit parameters for $M_{\rm gas}$ vs M_{Δ} at 24 different redshifts on the x-axis, from two catalogues B ($M_{\rm gas}$ vs M_{200}) and C ($M_{\rm gas}$ vs M_{500}) in the left and right columns respectively. The intercept, α, is shown in the top two graphs, where the y-axis is α normalised by the result at redshift zero and self-similar model prediction is represented by the black line . The slopes, β, are plotted in the middle two graphs, with the self-similar model prediction represented by the black line. The bottom graphs are the scatter, σ, from each redshift.

When breaking down the results into the fit parameters, see table 5.4, the normalisation, α, only evolves very weakly with redshift, with the C catalogue showing only a slightly stronger evolution. The slopes, β, tend away from the self-similar model prediction as redshift decreases, however, this evolution is only slight. This implies that AGN feedback is heating the gas and expanding it, leading to lower gas

fractions in lower mass clusters, this effect smooths out the $M_{\rm gas}$-Mass relation.

Scaling relation	Redshift	$(\alpha/\alpha_0)_{\rm B}$	$(\alpha/\alpha_0)_{\rm C}$	$\beta_{\rm B}$	$\beta_{\rm C}$	$\sigma_{\rm B}$	$\sigma_{\rm C}$
$M_{\rm gas}$ vs M_Δ	0.0	1.00	1.00	1.10	1.13	0.05	0.06
$M_{\rm gas}$ vs M_Δ	0.5	1.09	1.12	1.04	1.10	0.04	0.05
$M_{\rm gas}$ vs M_Δ	1.0	1.13	1.20	1.01	1.03	0.03	0.04

Table 5.4: Fit parameters for the scaling relations which relate gas mass to mass, where $(\alpha/\alpha_0)_{\rm B}$ is α normalised by α at redshift zero, α_0, for catalogue B and $(\alpha/\alpha_0)_{\rm C}$ is α normalised by α at redshift zero for catalogue C.

The scatter, σ, decreases as redshift increases, contrary to all the other relations. This is caused by the reduction in the range of masses of clusters, because as redshift increases the number of clusters decreases and more importantly the total mass of clusters decreases. So since the $M_{\rm gas}$-Mass relation is based on the fraction of the total mass which is gas and the total mass, the scatter decreases.

5.2.4 Y-Mass relations

Here we present the results from the Y-Mass relations. Figure 5.11 shows the best fit lines for $Y_{\rm X} - M_\Delta$ and $Y_{\rm SZ} - M_\Delta$ at three redshifts. The best fit lines are shorter as redshift increases because there are fewer high mass clusters at high redshifts, due to the time taken for clusters to accrue mass and a lower cluster count. There is little evolution in the $Y_{\rm SZ} - M_\Delta$best fit lines and even less in the $Y_{\rm X} - M_\Delta$. As self-similar evolution has been removed, from the best fit lines this means that the best fit lines agree with the self-similar model.

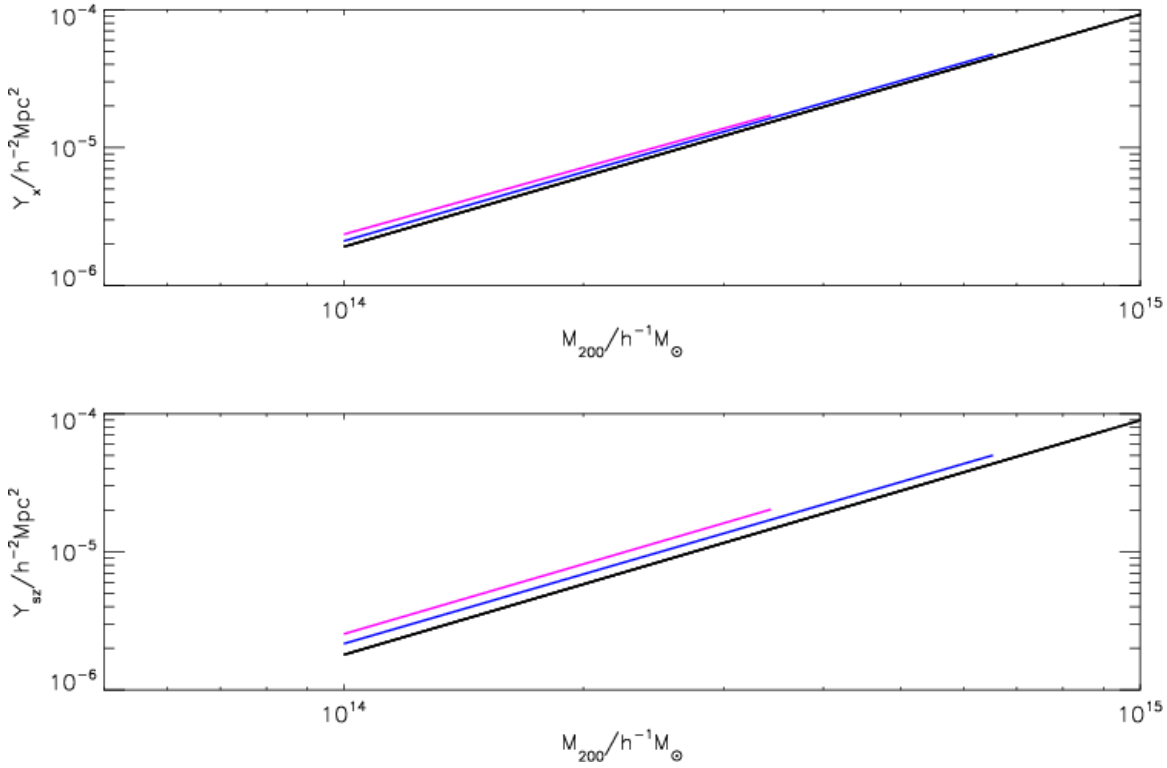

Figure 5.11: This figure shows the best fit line at redshift 0, 0.5, and 1 for the scaling relations that relate the Y parameter to mass, $Y_{\rm X} - M_{200}$ and $Y_{\rm SZ} - M_{200}$ respectively. The black line represents the result at redshift zero, the blue line redshift 1/2 and pink for redshift one.

These next graphs are the result of examining whether or not the fit parameters of the scaling relations evolve over redshift.

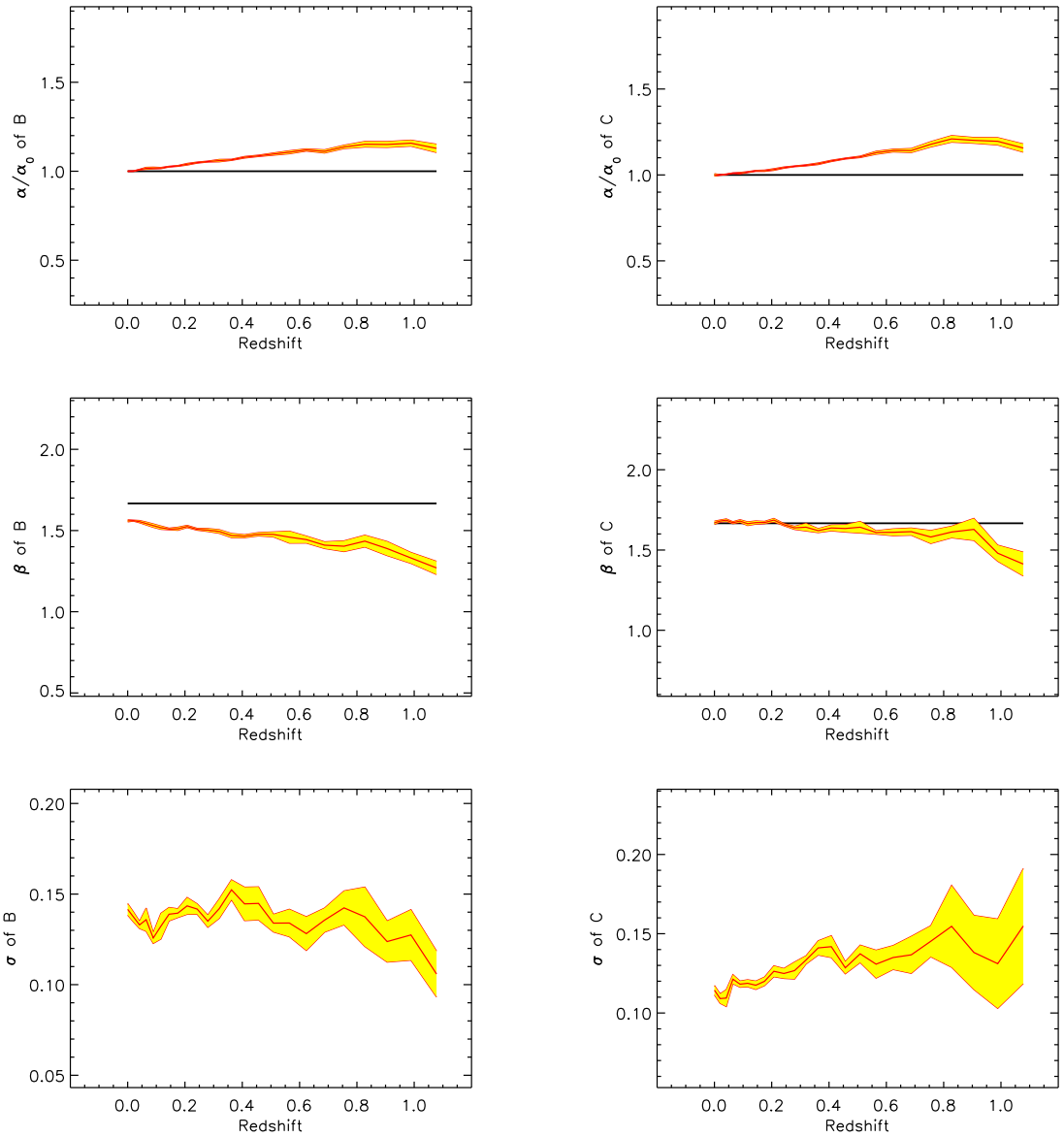

Figure 5.12: This figure shows the fit parameters for $Y_{\rm X}/E(z)^{2/3}$ vs M_{Δ} at 24 different redshifts on the x-axis, from two catalogues B ($Y_{\rm X}/E(z)^{2/3}$ vs M_{200}) and C ($Y_{\rm X}/E(z)^{2/3}$ vs M_{500}) in the left and right columns respectively. The intercept, α, is shown in the top two graphs, where the y-axis is α normalised by the result at redshift zero and the self-similar model prediction is represented by the black line . The slopes, β, are plotted in the middle two graphs, with the self-similar model prediction represented by the black line. The bottom graphs are the scatter, σ, from each redshift. All subsequent figures in this section follow the same layout.

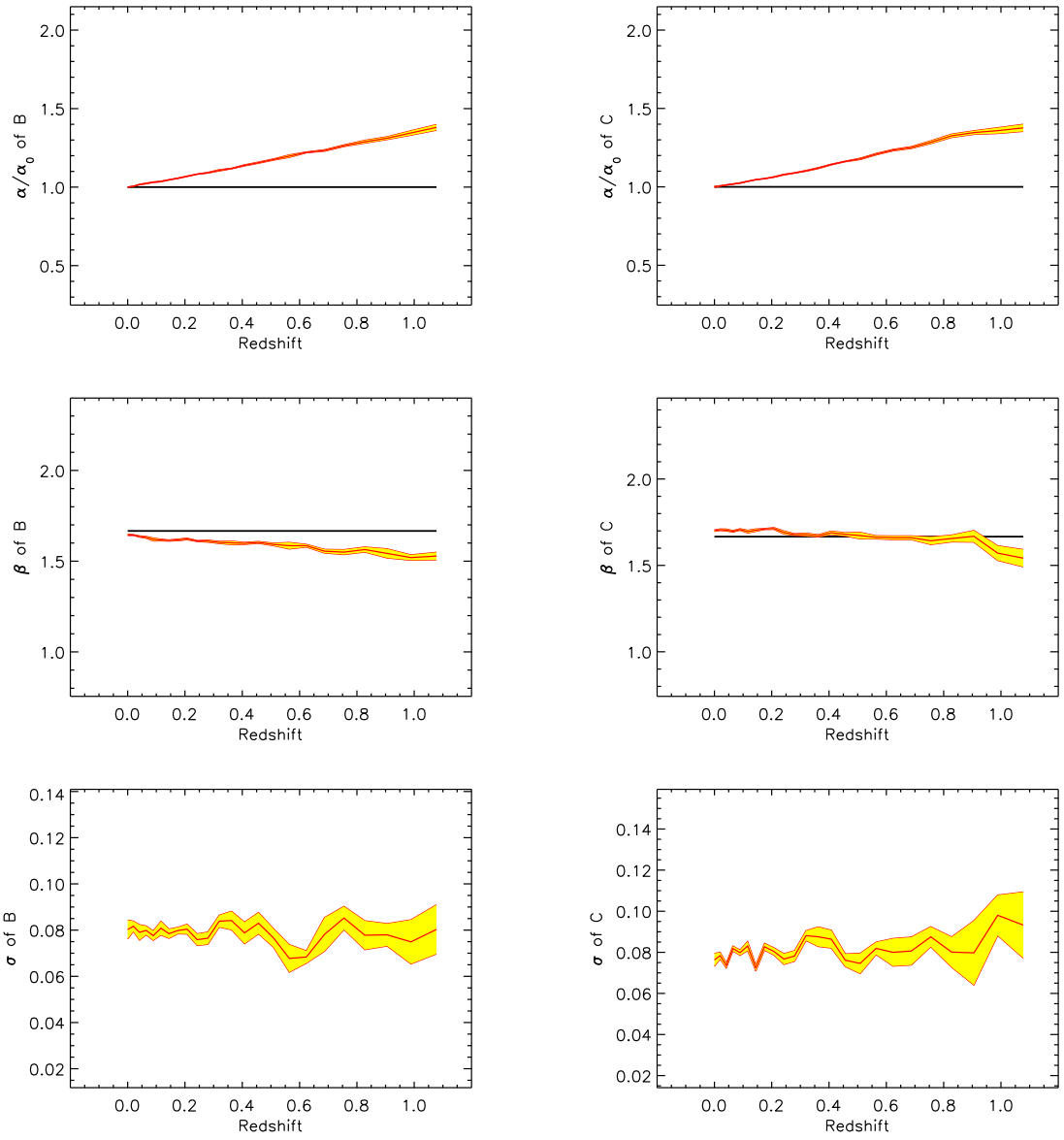

Figure 5.13: This figure shows the fit parameters for $Y_{\rm SZ}/E(z)^{2/3}$ vs M_Δ at 24 different redshifts from two catalogues B ($Y_{\rm SZ}/E(z)^{2/3}$ vs M_{200}) and C ($Y_{\rm SZ}/E(z)^{2/3}$ vs M_{500}) in the left and right columns respectively.

Table 5.5, is a summary of graphs 5.12 and 5.13. We find that the normalisations for $Y_{\rm X} - M_\Delta$ shows very little evolution in either the B or the C catalogue. However, there is a slight evolution in the normalisation for the $Y_{\rm SZ} - M_\Delta$ relation. This may be caused by the results from $T_{\rm m} - M_\Delta$ relation, see section 5.2.2, as $Y_{\rm SZ} - M_\Delta$ is dependent on the results from the $M_{\rm gas} - M_\Delta$ and $T_{\rm m} - M_\Delta$ relations. This may also account for the low scatter of this relation, σ, as both of the reliant relations are calculated from the mass content. On the other hand, the less flat and more scattered result for $Y_{\rm X} - M_{200}$ is due to the flat result from $T_{\rm sl} - M_\Delta$ relation.

Scaling relation	Redshift	$(\alpha/\alpha_0)_{\rm B}$	$(\alpha/\alpha_0)_{\rm C}$	$\beta_{\rm B}$	$\beta_{\rm C}$	$\sigma_{\rm B}$	$\sigma_{\rm C}$
$Y_{\rm X}$ vs M_Δ	0.0	1.00	1.00	1.56	1.67	0.14	0.11
$Y_{\rm X}$ vs M_Δ	0.5	1.10	1.11	1.48	1.64	0.13	0.14
$Y_{\rm X}$ vs M_Δ	1.0	1.13	1.16	1.27	1.41	0.11	0.15
$Y_{\rm SZ}$ vs M_Δ	0.0	1.00	1.00	1.65	1.70	0.08	0.08
$Y_{\rm SZ}$ vs M_Δ	0.5	1.18	1.18	1.59	1.67	0.08	0.07
$Y_{\rm SZ}$ vs M_Δ	1.0	1.38	1.38	1.53	1.54	0.08	0.09

Table 5.5: Fit parameters for the scaling relations which relate the Y parameter to mass, where $(\alpha/\alpha_0)_{\rm B}$ is α normalised by α at redshift zero, α_0, for catalogue B and $(\alpha/\alpha_0)_{\rm C}$ is α normalised by α at redshift zero for catalogue C.

When looking at the slopes, β, the $Y_{\rm X} - M_\Delta$ relation from catalogue B is never self-similar and tends away from the self-similar prediction, whereas the $Y_{\rm X} - M_\Delta$ relation from catalogue C is close to the self-similar model until redshift one. This result is repeated in the $Y_{\rm SZ} - M_\Delta$ relation, however, again it is flatter and slightly closer to the self-similar prediction for the same reasons as before.

5.2.5 Luminosity-Temperature relations

One of the reasons to include the L-T results, is to compare our results from the NMGS with the observational results from [Hilton et al., 2012]. [Hilton et al., 2012] take their data from XMM Cluster Survey and they find a negative evolution of the normalisation of the $L_{\rm bol} - T_{\rm sl}$ relation, which favours models with energy injection at high redshift. Negative evolution of the normalisation, means that the redshift evolution of the normalisation is weaker than self similar. Therefore, if the normalisation is plotted against redshift, the normalisation should be equal to one at redshift zero, the same as the self-similar result, but below one at higher redshift.

The NMGS simulates AGN feedback at all redshifts, unlike the [Hilton et al., 2012] models. Most of the energy injection in the NMGS occurs at low redshift where AGN feedback is more effective, as seen in figure 5.14.

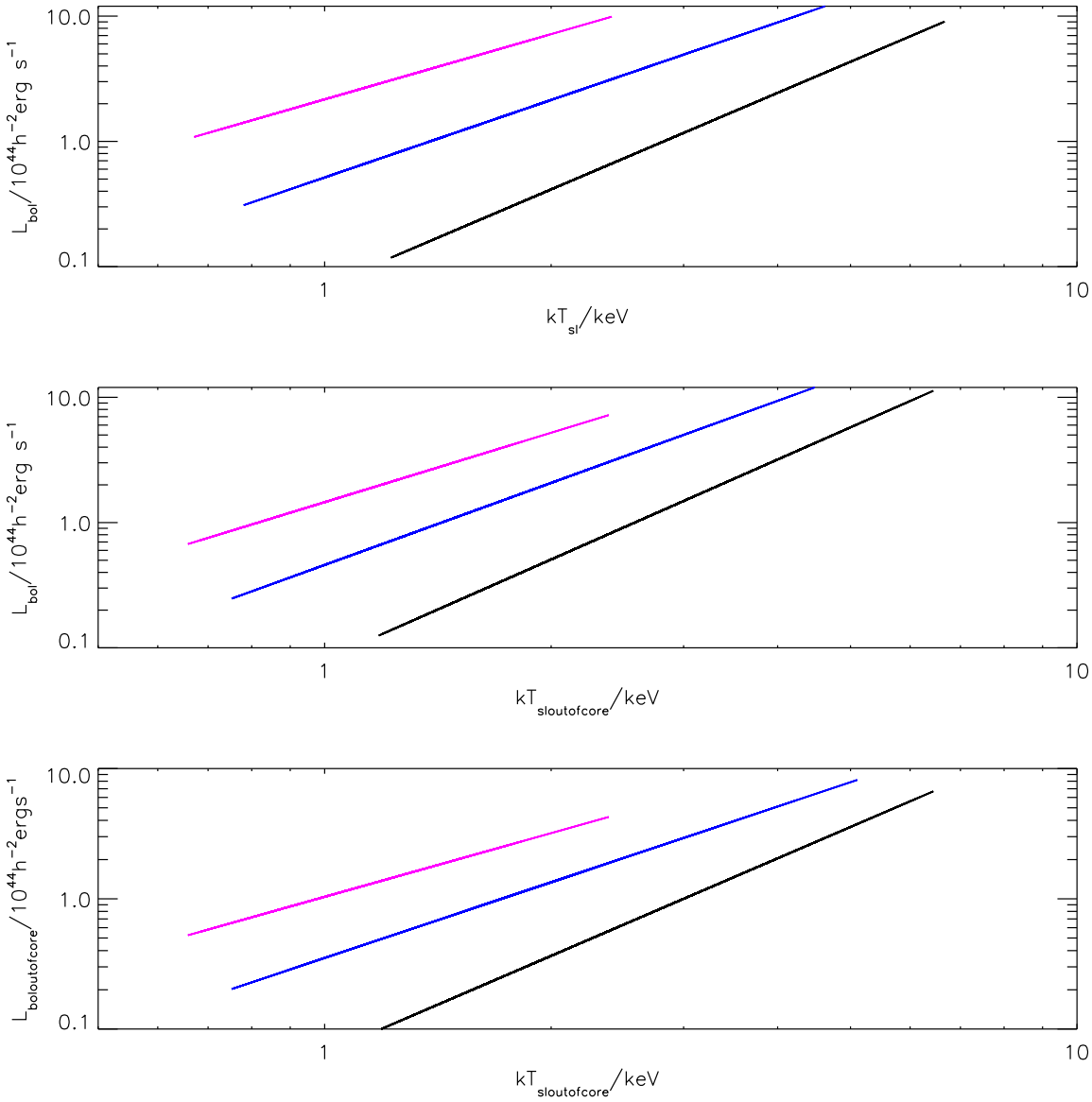

Figure 5.14: This figure shows the best fit line at redshift 0, 0.5, and 1 for the scaling relations that relate luminosity to temperature, $L_{\rm bol} - T_{\rm sl}$, $L_{\rm bol} - T_{\rm sloutofcore}$ and $L_{\rm boloutofcore} - T_{\rm sloutofcore}$ respectively. The black line represents the result at redshift zero, the blue line redshift 1/2 and pink for redshift one.

Figure 5.14 shows the best fit lines for the luminosity temperature relations at three redshifts, which were taken from catalogue B. The best fit lines have much smaller temperature ranges as redshift increases, due to the time taken for clusters to accrue mass and a lower cluster count. Here there is an obvious evolution away from the result at redshift zero, for all the relations. This disagrees with the self-similar prediction, as self-similar evolution has been factored out of these lines best fit. Indeed, for all three relations we see a lower temperature and an increase in

luminosity then predicted at higher redshift. This is caused by the AGN feedback, for as the redshift decreases the effect of AGN feedback increases which causes the ICM to get hotter and less dense; this leads to an increase in temperature and a decrease in luminosity. Table 5.6 shows the fit parameters for the same relations, whose fit parameters are shown below.

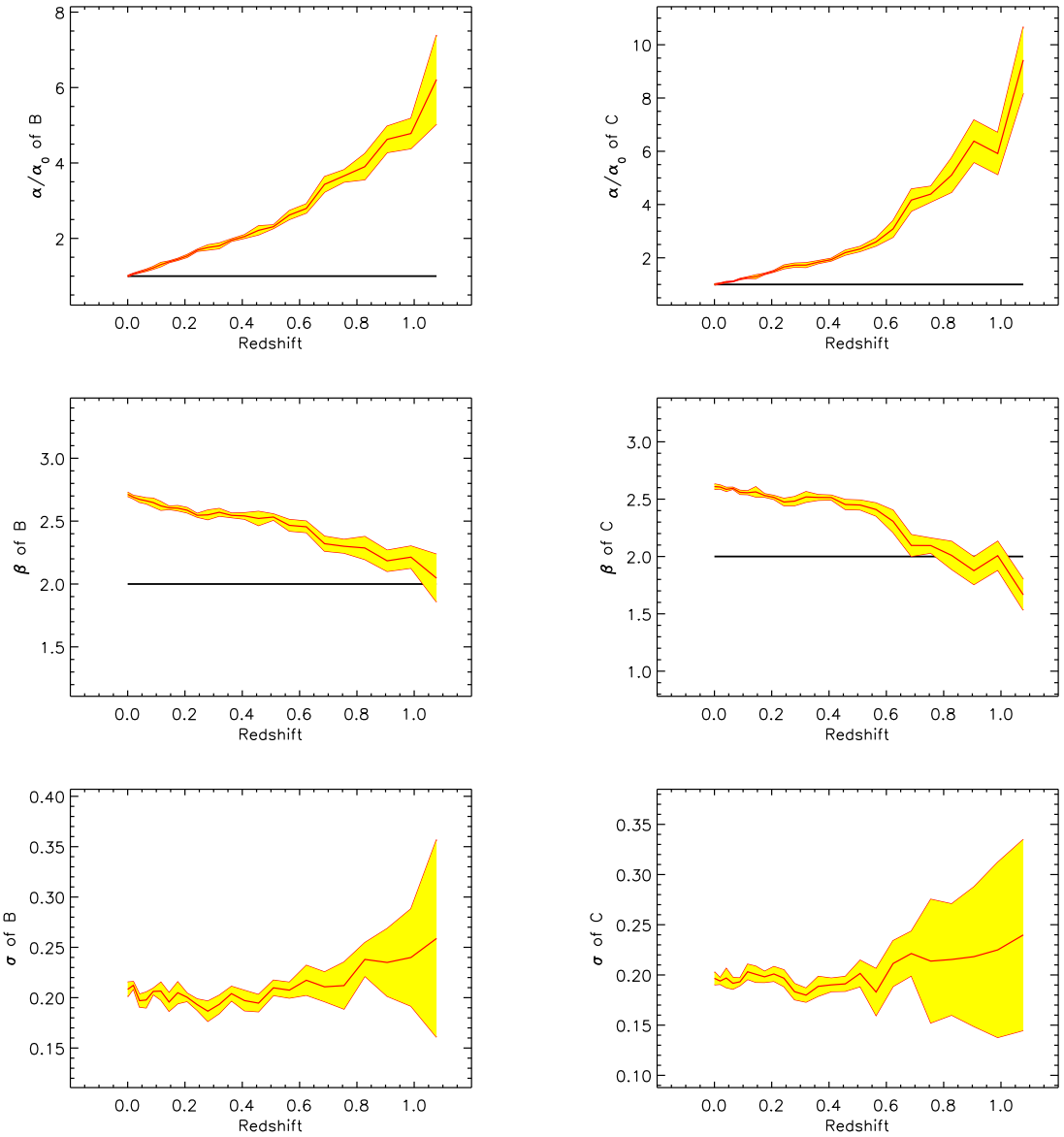

Figure 5.15: This figure shows the fit parameters for $L_{\rm bol}/E(z)$ vs $T_{\rm sl}$ at 24 different redshifts on the x-axis, from two catalogues B ($L_{\rm bol}/E(z)$ vs $T_{\rm sl}$) and C ($L_{\rm bol}/E(z)$ vs $T_{\rm sl}$) in the left and right columns respectively. The red line in the centre being the value of that fit parameter at that redshift, the yellow representing the error for each result and the red lines on the outside are the limits of those errors. The intercept, α, is shown in the top two graphs, where the y-axis is α normalised by the result at redshift zero and the self-similar model prediction is represented by the black line. The slopes, β, are plotted in the middle two graphs, with the self-similar model prediction represented by the black line. The bottom graphs are the scatter, σ, from each redshift. All subsequent figures in this section follow the same layout.

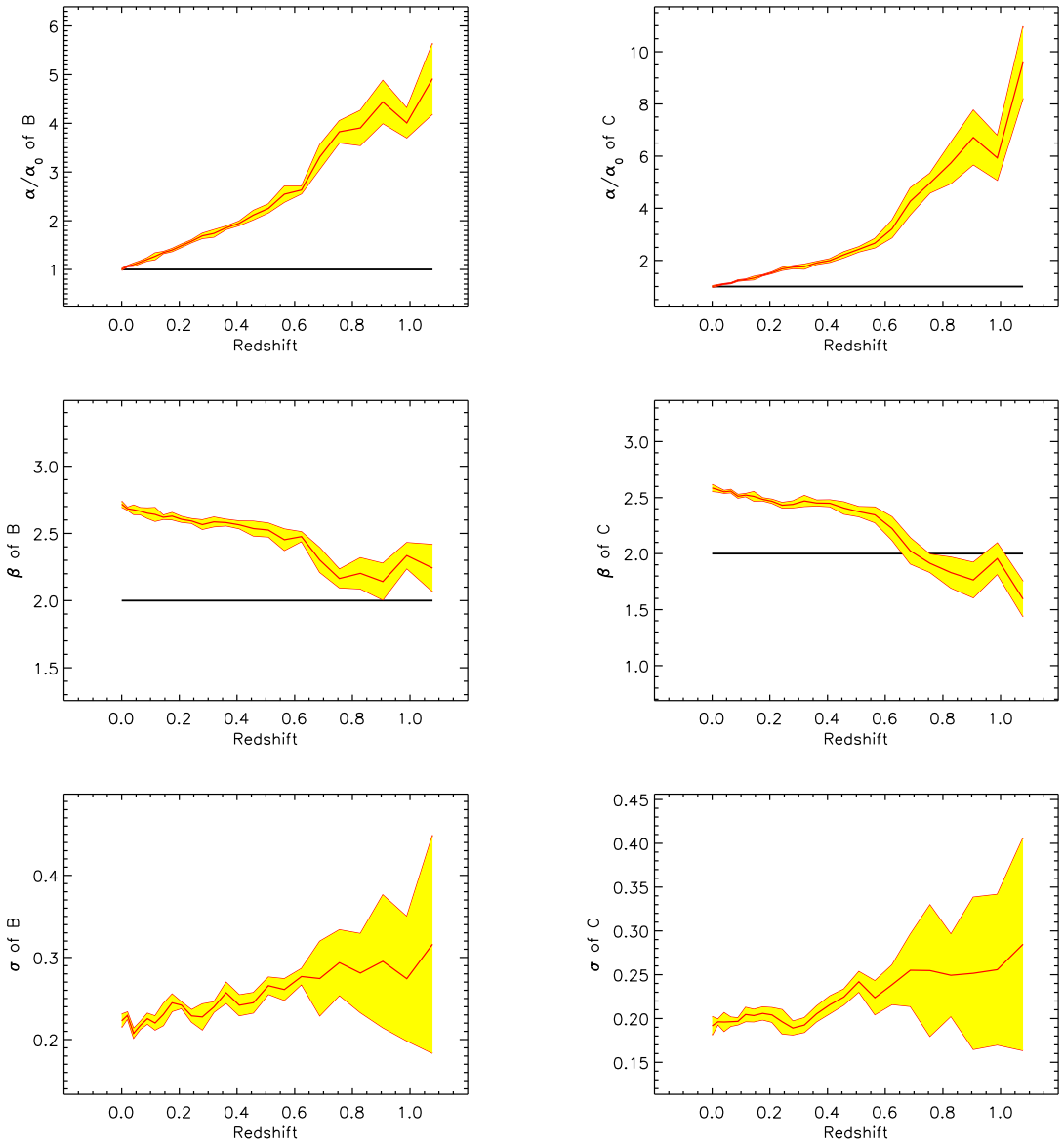

Figure 5.16: This figure shows the fit parameters for $L_{\rm boloutcore}/E(z)$ vs $T_{\rm sl}$ at 24 different redshifts from two catalogues B ($L_{\rm boloutcore}/E(z)$ vs $T_{\rm sl}$) and C ($L_{\rm boloutcore}/E(z)$ vs $T_{\rm sl}$) in the left and right columns respectively.

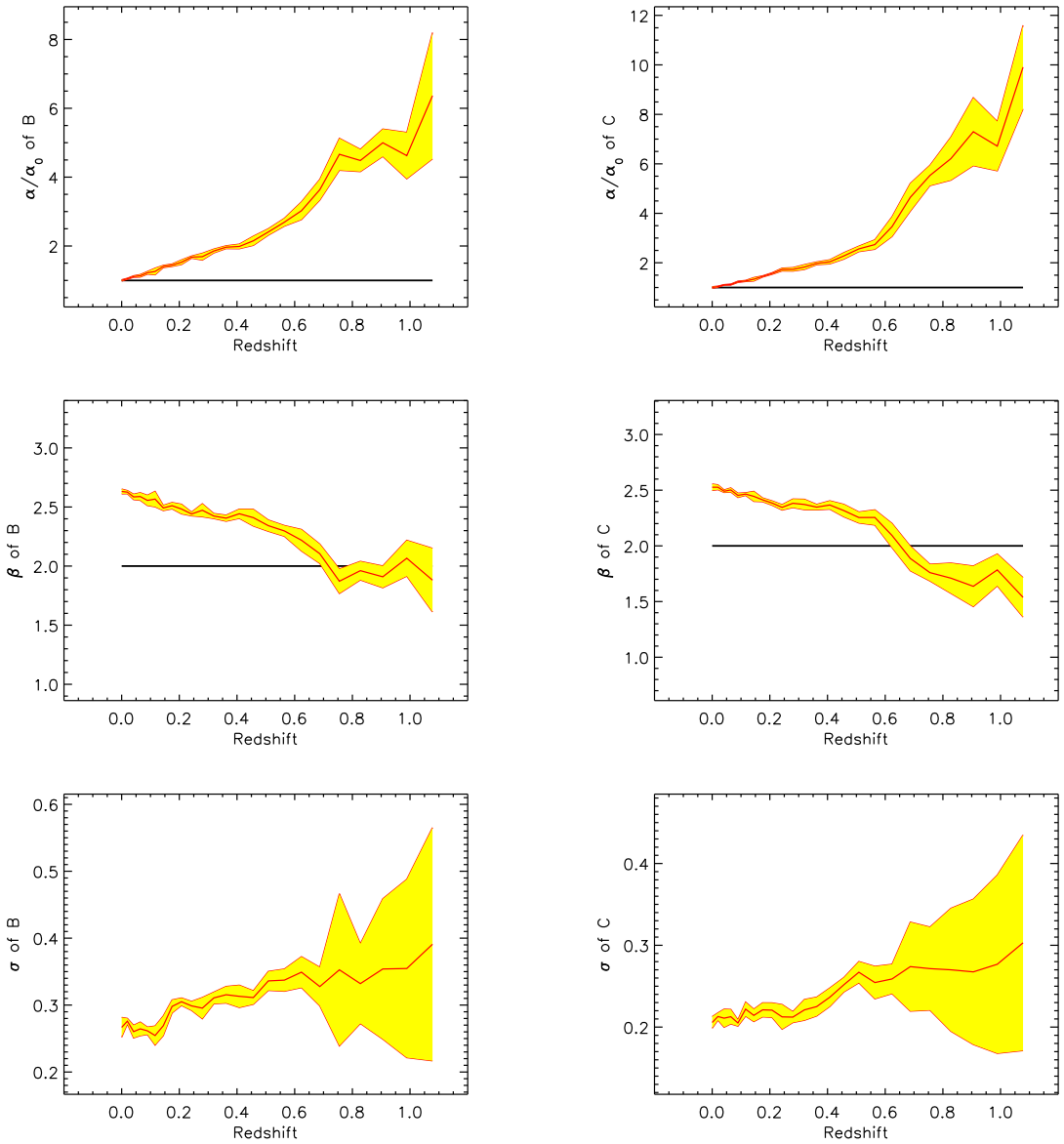

Figure 5.17: This figure shows the fit parameters for $L_{\rm boloutcore}/E(z)$ vs $T_{sloutcore}$ at 24 different redshifts from two catalogues B ($L_{\rm boloutcore}/E(z)$ vs $T_{\rm sloutcore}$) and C ($L_{\rm boloutcore}/E(z)$ vs $T_{\rm sloutcore}$) in the left and right columns respectively.

Table 5.6 provides a summary at three redshifts of the fit parameters from the graphs 5.15, 5.16 and 5.17. We find that the normalisation, α, in catalogue B evolves away from the self-similar prediction, however, the $L_{\rm bol} - T_{\rm sloutofcore}$ shows a slightly slower evolution than the other two relations. In the C catalogue, the normalisations tend to evolve faster and at a similar rate, which is interesting as AGN heating occurs mostly in the core of the cluster. We would expect that once we exclude the core the temperature would decrease, however, that is not seen the C catalogue. This maybe caused by the lower cluster count at redshift one for the

Scaling relation	Redshift	$(\alpha/\alpha_0)_B$	$(\alpha/\alpha_0)_C$	β_B	β_C	σ_B	σ_C
L_{bol} vs T_{sl}	0.0	1.00	1.00	2.71	2.61	0.21	0.20
L_{bol} vs T_{sl}	0.5	2.31	2.33	2.53	2.45	0.21	0.20
L_{bol} vs T_{sl}	1.0	6.21	9.43	2.05	1.67	0.26	0.24
L_{bol} vs $T_{sloutofcore}$	0.0	1.00	1.00	2.72	2.59	0.22	0.19
L_{bol} vs $T_{sloutofcore}$	0.5	2.25	2.43	2.53	2.37	0.27	0.24
L_{bol} vs $T_{sloutofcore}$	1.0	4.92	9.60	2.24	1.59	0.32	0.28
$L_{boloutofcore}$ vs $T_{sloutofcore}$	0.0	1.00	1.00	2.63	2.53	0.27	0.21
$L_{boloutofcore}$ vs $T_{sloutofcore}$	0.5	2.41	2.56	2.34	2.25	0.34	0.27
$L_{boloutofcore}$ vs $T_{sloutofcore}$	1.0	6.37	9.91	1.88	1.54	0.39	0.30

Table 5.6: Fit parameters for the scaling relations which relate the luminosity to mass, where $(\alpha/\alpha_0)_B$ is α normalised by α at redshift zero, α_0, for catalogue B and $(\alpha/\alpha_0)_C$ is α normalised by α at redshift zero for catalogue C.

C catalogue, which is only 64.

When comparing the simulated slopes to the observed data from [Hilton et al., 2012], we find evolution the $L_{bol} - T_{sl}$ relation, where they do not. Furthermore, we find a positive evolution in the normalisation, which agrees with their simulated data, of a 250 Mpc/h box, but again, not with their observed data. This may be due to the XMM Cluster Survey first data release, XCS-DR1 data, from which [Hilton et al., 2012] takes their data. XCS-DR1 favours feedback models with energy injection high redshift. However, the NMGS injects feedback at all redshifts which may cause this discrepancy.

We also find that the slopes, β, of the L-T relations (in both catalogues) tend to deviate from the self-similar model at low redshifts, but then approach the self-similar prediction at higher redshift. When removing the luminosity from the clusters' cores, $L_{boloutcore} - T_{sl}$, the relation no longer shows a tendency to the self-similar prediction, however, removing both the luminosity and the temperature from the clusters' cores restores the tendency to self-similarity. This shows that the NMGS agrees with the self-similar model at high redshift, but in the run up to redshift zero, the scaling relations tend to evolve away from the self-similar model.

5.2.6 Overview

From the previous graphs, it is clear that, as redshift increases the error in all the fit parameters increases, this is due to the decrease in cluster count with increasing redshift. This is also seen in the σ as well, more deviation from the line of best fit, which shows that our estimate of σ becomes more uncertain as redshift increases. This verifies the methodology, for this is what was expected with a lower cluster count.

The normalised scaling relations seem to evolve negatively with respect to the self-similar slope, with $T_{\rm m}$ being the weakest with cosmology; [Vikhlinin et al., 2009] find a similar result. When comparing to previous theoretical work, [Short et al., 2010] finds positive evolution in their FO model for $Y_{\rm X} - M$, $L_{\rm bol} - M$ and $L_{\rm bol} - T_{\rm sl}$. This may be due to the more accurate prediction of AGN feedback found in in the NMGS.

[Kay et al., 2012] finds a flatter evolution for the $Y_{\rm X} - M$ relation. Our results show a more negative evolution. This maybe due to the use of a different cosmological model.

Previous simulations which provide redshift data of the same scaling relations suggested that AGN heating was required at higher redshift to account for the scaling relations evolution as seen in these models. This result agrees with observational data from [Böhringer et al., 2012]. This is what our results have shown, because most of the scaling relations tend to the self-similar model at high redshift. A couple of exceptions occur in the $Y_{\rm X}$ and $T_{\rm sl}$ case. Interestingly, the results excluding the core in figure 5.3 seem to evolve onto from the self-similar slope. We still, however, find a divergence from the self-similar model, in section 5.2.5.

Chapter 6

Conclusion

6.1 Summary

This thesis has presented results from the analysis of cluster scaling relations, using a new cosmological simulation which includes the effects of feedback from AGN. Cluster scaling relations are used with the mass function to constrain cosmological parameters. Starting from the basic assumption that the scaling relations are self-similar and that the only important physical process is gravity, simple predictions (power-law relations) for the scaling relations can be made. Through reviewing observational determinations, we can show that these relations are do not agree with the self-similar predictions. This is caused by non-gravitational physics, with AGN feedback being the largest problem. We model AGN feedback through a new, large, cosmological hydrodynamical simulation. Then we compare the scaling relations at redshift zero with observations, before investigating their evolution with redshift.

Our data, at redshift zero, predict:

- Lower mass clusters have lower luminosity than expected, due to the feedback from AGN. This leads to a steeper $L_{\rm bol} - M_{\Delta}$ and $L_{\rm bol} - T_{\rm sl}$ than predicted by the self-similar model.

- Comparing the mass-weighted and spectroscopic-like temperatures, our results suggest that the ICM is not particularly clumpy in the simulation.

- The $M_{\rm gas}$ relation suggests that the feedback heats the ICM and expands it, leading to a lower gas fraction in lower mass clusters.

- The Y parameter relations are only slightly steeper than the self-similar model prediction. The increase in the temperature of the ICM by feedback is partly offset by the decrease in the $M_{\rm gas}$ relation.

We then test the scaling relations at higher redshifts. Here we have compared our results to the self-similar model, which predicts no evolution in the slopes of the relations. We find that most of the scaling relations show evolution in both slope and normalisation. However, the temperature and the Y parameter relations show no evolution in either.

6.2 Future research

Since modelling cluster scaling relations can be used to constrain cosmological parameters, future observations coupled with results from newer simulations will provide new insights into cosmology. Give the limited time available, further analysis on the scaling relations would include:

- Correlation fitting, similar to the redshift zero results, could have been performed on the scaling relations at each redshift, to further analyse the interdependence of the scaling relations.

- Since the scaling relations are interdependent, more analysis could be done to break down them into interrelated parts. The effect of individual cluster properties could then be more effectively analysed.

- The higher redshifted data could have been compared to observational results to see if our simulation agrees with observations at higher redshifts.

- A quadratic fit to the scaling relations could have been used instead of a linear one, to see if that would better fit the data.

It is clear that in order to use clusters to measure cosmological parameters, it is important that the scaling relations are accurately measured as a function of redshift, as it is not simple to predict them from a physical model.

Appendix A

Appendix

A.1 Other catalogues at redshift zero

Other catalogues at redshift zero are shown, for completeness, here.

Scaling relation	$log_e(\alpha)$	β	σ
$L_{\rm bol}$	-0.08 ± 0.009	1.29 ± 0.024	0.27± 0.012
$L_{\rm boloutcore}$	-0.68 ± 0.007	1.43 ± 0.018	0.16 ± 0.007
$T_{\rm m}$	0.78 ± 0.002	0.54 ± 0.007	0.08 ±0.002
$T_{\rm sl}$	0.95 ± 0.004	0.42 ± 0.012	0.13± 0.006
$T_{\rm sloutcore}$	0.79 ± 0.004	0.46 ± 0.011	0.11 ± 0.005
$M_{\rm gas}$	31.2 ± 0.001	1.05 ± 0.003	0.05 ± 0.001
$Y_{\rm X}$	-11.6 ± 0.005	1.47 ± 0.013	0.15 ± 0.006
$Y_{\rm SZ}$	-11.7 ± 0.003	1.60 ± 0.008	0.09 ± 0.004
Q	1.40 ± 0.008	0.06 ± 0.019	0.21 ± 0.009

Table A.1: Fit parameters for the A catalogue, with a cluster count of 810 and 10,000 realisations used with a pivot mass of 2.70×10^{14} solar masses. Relations are in the form of $O \propto M_{vir}$.

Scaling relation	$\log_e(\alpha)$	β	σ
$L_{\rm bol}$	-0.24 ± 0.009	1.37 ± 0.021	0.26 ± 0.010
$L_{\rm boloutcore}$	-0.66 ± 0.006	1.47 ± 0.015	0.16 ± 0.007
$T_{\rm m}$	0.84 ± 0.002	0.54 ± 0.006	0.07 ± 0.002
$T_{\rm sl}$	0.94 ± 0.004	0.45 ± 0.010	0.12 ± 0.005
$T_{\rm sloutcore}$	0.84 ± 0.003	0.48 ± 0.009	0.10 ± 0.004
$M_{\rm gas}$	30.9 ± 0.002	1.09 ± 0.003	0.06 ± 0.001
$Y_{\rm X}$	-11.9 ± 0.005	1.55 ± 0.011	0.14 ± 0.006
$Y_{\rm SZ}$	-12.0 ± 0.003	1.64 ± 0.006	0.09 ± 0.003
Q	1.03 ± 0.007	0.06 ± 0.016	0.19 ± 0.008

Table A.2: Fit parameters for the F catalogue, with a cluster count of 921 and 10,000 realisations used with a pivot mass of 2.05×10^{14} solar masses. Relations are in the form of $O \propto M_{180}$.

Scaling relation	$\log_e(\alpha)$	β	σ
$L_{\rm bol}$	0.35 ± 0.012	1.41 ± 0.042	0.18 ± 0.015
$L_{\rm boloutcore}$	0.22 ± 0.011	1.45 ± 0.036	0.14 ± 0.012
$T_{\rm m}$	1.35 ± 0.004	0.60 ± 0.011	0.06 ± 0.004
$T_{\rm sl}$	1.33 ± 0.004	0.55 ± 0.011	0.07 ± 0.003
$T_{\rm sloutcore}$	1.31 ± 0.003	0.56 ± 0.012	0.06 ± 0.003
$M_{\rm gas}$	30.4 ± 0.003	1.10 ± 0.012	0.06 ± 0.003
$Y_{\rm X}$	-12.0 ± 0.005	1.65 ± 0.017	0.09 ± 0.007
$Y_{\rm SZ}$	-12.0 ± 0.006	1.70 ± 0.016	0.08 ± 0.006
Q	0.43 ± 0.009	0.01 ± 0.027	0.13 ± 0.011

Table A.3: Fit parameters for the D catalogue, with a cluster count of 264 and 10,000 realisations used with a pivot mass of 1.45×10^{14} solar masses. Relations are in the form of $O \propto M_{1000}$.

Scaling relation	$\log_e(\alpha)$	β	σ
$L_{\rm bol}$	1.45 ± 0.057	1.50 ± 0.272	0.12 ± 0.038
$L_{\rm boloutcore}$	1.37 ± 0.060	1.50 ± 0.291	0.10 ± 0.042
$T_{\rm m}$	1.88 ± 0.023	0.59 ± 0.135	0.05 ± 0.025
$T_{\rm sl}$	1.84 ± 0.013	0.62 ± 0.073	0.03 ± 0.013
$T_{\rm sloutcore}$	1.83 ± 0.013	0.62 ± 0.075	0.03 ± 0.014
$M_{\rm gas}$	30.5 ± 0.018	1.12 ± 0.098	0.05 ± 0.024
$Y_{\rm X}$	-11.4 ± 0.025	1.74 ± 0.146	0.04 ± 0.023
$Y_{\rm SZ}$	-11.3 ± 0.035	1.70 ± 0.189	0.05 ± 0.044
Q	0.30 ± 0.022	0.02 ± 0.118	0.08 ± 0.024

Table A.4: Fit parameters for the E catalogue, with a cluster count of 15 and 10,000 realisations used with a pivot mass of 1.68×10^{14} solar masses. Relations are in the form of $O \propto M_{2500}$.

Bibliography

M. Arnaud and A. E. Evrard. The L_X-T relation and intracluster gas fractions of X-ray clusters. MNRAS, 305:631–640, May 1999. doi: 10.1046/j.1365-8711.1999.02442.x.

M. Arnaud, E. Pointecouteau, and G. W. Pratt. The structural and scaling properties of nearby galaxy clusters. II. The M-T relation. A&A, 441:893–903, October 2005. doi: 10.1051/0004-6361:20052856.

M. L. Balogh, F. R. Pearce, R. G. Bower, and S. T. Kay. Revisiting the cosmic cooling crisis. MNRAS, 326:1228–1234, October 2001. doi: 10.1111/j.1365-8711.2001.04667.x.

C. M. Baugh. A primer on hierarchical galaxy formation: the semi-analytical approach. *Reports on Progress in Physics*, 69:3101–3156, December 2006. doi: 10.1088/0034-4885/69/12/R02.

H. Böhringer, K. Matsushita, E. Churazov, Y. Ikebe, and Y. Chen. The new emerging model for the structure of cooling cores in clusters of galaxies. A&A, 382:804–820, February 2002. doi: 10.1051/0004-6361:20011708.

H. Böhringer, K. Dolag, and G. Chon. Modelling self-similar appearance of galaxy clusters in X-rays. A&A, 539:A120, March 2012. doi: 10.1051/0004-6361/201118000.

S. Borgani, G. Murante, V. Springel, A. Diaferio, K. Dolag, L. Moscardini, G. Tormen, L. Tornatore, and P. Tozzi. X-ray properties of galaxy clusters and groups

from a cosmological hydrodynamical simulation. MNRAS, 348:1078–1096, March 2004. doi: 10.1111/j.1365-2966.2004.07431.x.

S. Borgani, K. Dolag, G. Murante, L.-M. Cheng, V. Springel, A. Diaferio, L. Moscardini, G. Tormen, L. Tornatore, and P. Tozzi. Hot and cooled baryons in smoothed particle hydrodynamic simulations of galaxy clusters: physics and numerics. MNRAS, 367:1641–1654, April 2006. doi: 10.1111/j.1365-2966.2006.10075.x.

R. J. Bouwens, G. D. Illingworth, P. A. Oesch, M. Stiavelli, P. van Dokkum, M. Trenti, D. Magee, I. Labb, M. Franx, C. M. Carollo, and V. Gonzalez. Discovery of z 8 galaxies in the hubble ultra deep field from ultra-deep wfc3/ir observations. *The Astrophysical Journal Letters*, 709(2):L133, 2010. URL `http://stacks.iop.org/2041-8205/709/i=2/a=L133`.

G. L. Bryan. Explaining the Entropy Excess in Clusters and Groups of Galaxies without Additional Heating. ApJ, 544:L1–L5, November 2000. doi: 10.1086/317289.

G. L. Bryan and M. L. Norman. Statistical Properties of X-Ray Clusters: Analytic and Numerical Comparisons. ApJ, 495:80–99, March 1998. doi: 10.1086/305262.

I.-N. T. Chiu and S. M. Molnar. Testing Hydrostatic Equilibrium in Galaxy Cluster MS 2137. ApJ, 756:1, September 2012. doi: 10.1088/0004-637X/756/1/1.

D. Coe, A. Zitrin, M. Carrasco, X. Shu, W. Zheng, M. Postman, L. Bradley, A. Koekemoer, R. Bouwens, T. Broadhurst, A. Monna, O. Host, L. A. Moustakas, H. Ford, J. Moustakas, A. van der Wel, M. Donahue, S. A. Rodney, N. Benitez, S. Jouvel, S. Seitz, D. D. Kelson, and P. Rosati. CLASH: Three Strongly Lensed Images of a Candidate z ˜ 11 Galaxy. *ArXiv e-prints*, November 2012.

S. Cole, C. G. Lacey, C. M. Baugh, and C. S. Frenk. Hierarchical galaxy formation. MNRAS, 319:168–204, November 2000. doi: 10.1046/j.1365-8711.2000.03879.x.

R. Davé, B. D. Oppenheimer, and S. Sivanandam. Enrichment and pre-heating in

intragroup gas from galactic outflows. MNRAS, 391:110–123, November 2008. doi: 10.1111/j.1365-2966.2008.13906.x.

L. P. David, A. Slyz, C. Jones, W. Forman, S. D. Vrtilek, and K. A. Arnaud. A catalog of intracluster gas temperatures. ApJ, 412:479–488, August 1993. doi: 10.1086/172936.

L. P. David, P. E. J. Nulsen, B. R. McNamara, W. Forman, C. Jones, T. Ponman, B. Robertson, and M. Wise. A High-Resolution Study of the Hydra A Cluster with Chandra: Comparison of the Core Mass Distribution with Theoretical Predictions and Evidence for Feedback in the Cooling Flow. ApJ, 557:546–559, August 2001. doi: 10.1086/322250.

J. P. Dietrich and J. Hartlap. Cosmology with the shear-peak statistics. MNRAS, 402:1049–1058, February 2010. doi: 10.1111/j.1365-2966.2009.15948.x.

H. J. Eckmiller, D. S. Hudson, and T. H. Reiprich. Testing the low-mass end of X-ray scaling relations with a sample of Chandra galaxy groups. A&A, 535:A105, November 2011. doi: 10.1051/0004-6361/201116734.

A. C. Edge, G. C. Stewart, A. C. Fabian, and K. A. Arnaud. An X-Ray Flux-Limited Sample of Clusters of Galaxies - Evidence for Evolution of the Luminosity Function. MNRAS, 245:559, July 1990.

V. R. Eke, S. Cole, and C. S. Frenk. Cluster evolution as a diagnostic for Omega. MNRAS, 282:263–280, September 1996.

S. Ettori and F. Brighenti. On the evolution of cooling cores in X-ray galaxy clusters. MNRAS, 387:631–638, June 2008. doi: 10.1111/j.1365-2966.2008.13054.x.

A. E. Evrard and J. P. Henry. Expectations for X-ray cluster observations by the ROSAT satellite. ApJ, 383:95–103, December 1991. doi: 10.1086/170767.

A. Finoguenov, T. H. Reiprich, and H. Böhringer. Details of the mass-temperature relation for clusters of galaxies. A&A, 368:749–759, March 2001. doi: 10.1051/0004-6361:20010080.

J. E. Gunn and J. R. Gott, III. On the Infall of Matter Into Clusters of Galaxies and Some Effects on Their Evolution. ApJ, 176:1, August 1972. doi: 10.1086/151605.

Q. Guo, S. White, M. Boylan-Kolchin, G. De Lucia, G. Kauffmann, G. Lemson, C. Li, V. Springel, and S. Weinmann. From dwarf spheroidals to cD galaxies: simulating the galaxy population in a ΛCDM cosmology. MNRAS, 413:101–131, May 2011. doi: 10.1111/j.1365-2966.2010.18114.x.

W. G. Hartley, L. Gazzola, F. R. Pearce, S. T. Kay, and P. A. Thomas. Nature versus nurture: the curved spine of the galaxy cluster X-ray luminosity-temperature relation. MNRAS, 386:2015–2021, June 2008. doi: 10.1111/j.1365-2966.2008.13127.x.

M. Hilton, A. K. Romer, S. T. Kay, N. Mehrtens, E. J. Lloyd-Davies, P. A. Thomas, C. J. Short, J. A. Mayers, P. J. Rooney, J. P. Stott, C. A. Collins, C. D. Harrison, B. Hoyle, A. R. Liddle, R. G. Mann, C. J. Miller, M. Sahlén, P. T. P. Viana, M. Davidson, M. Hosmer, R. C. Nichol, K. Sabirli, S. A. Stanford, and M. J. West. The XMM Cluster Survey: evidence for energy injection at high redshift from evolution of the X-ray luminosity-temperature relation. MNRAS, 424:2086–2096, August 2012. doi: 10.1111/j.1365-2966.2012.21359.x.

H. Hoekstra. A comparison of weak-lensing masses and X-ray properties of galaxy clusters. MNRAS, 379:317–330, July 2007. doi: 10.1111/j.1365-2966.2007.11951.x.

Y. Ikebe, T. H. Reiprich, H. Böhringer, Y. Tanaka, and T. Kitayama. A new measurement of the X-ray temperature function of clusters of galaxies. A&A, 383:773–790, March 2002. doi: 10.1051/0004-6361:20011769.

N. Kaiser. Evolution and clustering of rich clusters. MNRAS, 222:323–345, September 1986.

N. Kaiser. Evolution of clusters of galaxies. ApJ, 383:104–111, December 1991. doi: 10.1086/170768.

S. Kay. Galaxy Formation PHYS40922 [Lecture 21 notes]. *Frontiers of Galaxy Formation*, N-body simulations, April 2013.

S. T. Kay, P. A. Thomas, A. Jenkins, and F. R. Pearce. Cosmological simulations of the intracluster medium. MNRAS, 355:1091–1104, December 2004. doi: 10.1111/j.1365-2966.2004.08383.x.

S. T. Kay, M. W. Peel, C. J. Short, P. A. Thomas, O. E. Young, R. A. Battye, A. R. Liddle, and F. R. Pearce. Sunyaev-Zel'dovich clusters in Millennium gas simulations. MNRAS, 422:1999–2023, May 2012. doi: 10.1111/j.1365-2966.2012.20623.x.

A. V. Kravtsov and G. Yepes. On the supernova heating of the intergalactic medium. MNRAS, 318:227–238, October 2000. doi: 10.1046/j.1365-8711.2000.03771.x.

Andrey V. Kravtsov, Alexey Vikhlinin, and Daisuke Nagai. A new robust low-scatter x-ray mass indicator for clusters of galaxies. *The Astrophysical Journal*, 650(1): 128, 2006. URL `http://stacks.iop.org/0004-637X/650/i=1/a=128`.

M. Markevitch. The L X-T Relation and Temperature Function for Nearby Clusters Revisited. ApJ, 504:27, September 1998. doi: 10.1086/306080.

B. J. Maughan. The L_X-Y_X Relation: Using Galaxy Cluster X-Ray Luminosity as a Robust, Low-Scatter Mass Proxy. ApJ, 668:772–780, October 2007. doi: 10.1086/520831.

B. J. Maughan, L. R. Jones, H. Ebeling, and C. Scharf. The evolution of the cluster X-ray scaling relations in the Wide Angle ROSAT Pointed Survey sample at $0.6 < z < 1.0$. MNRAS, 365:509–529, January 2006. doi: 10.1111/j.1365-2966.2005.09717.x.

B. J. Maughan, P. A. Giles, S. W. Randall, C. Jones, and W. R. Forman. Self-similar scaling and evolution in the galaxy cluster X-ray luminosity-temperature relation. MNRAS, 421:1583–1602, April 2012. doi: 10.1111/j.1365-2966.2012.20419.x.

P. Mazzotta, E. Rasia, S. Borgani, L. Moscardini, K. Dolag, and G. Tormen. Spectroscopic-Like Temperature of Clusters of Galaxies and Cosmological Implications. *ArXiv Astrophysics e-prints*, December 2004.

B. R. McNamara and P. E. J. Nulsen. Heating Hot Atmospheres with Active Galactic Nuclei. ARA&A, 45:117–175, September 2007. doi: 10.1146/annurev.astro.45.051806.110625.

C. A. Metzler and A. E. Evrard. A simulation of the intracluster medium with feedback from cluster galaxies. ApJ, 437:564–583, December 1994. doi: 10.1086/175022.

J. J. Mohr, B. Mathiesen, and A. E. Evrard. Properties of the Intracluster Medium in an Ensemble of Nearby Galaxy Clusters. ApJ, 517:627–649, June 1999. doi: 10.1086/307227.

S. More, A. V. Kravtsov, N. Dalal, and S. Gottlöber. The Overdensity and Masses of the Friends-of-friends Halos and Universality of Halo Mass Function. ApJS, 195:4, July 2011. doi: 10.1088/0067-0049/195/1/4.

O. Muanwong, P. A. Thomas, S. T. Kay, F. R. Pearce, and H. M. P. Couchman. The Effect of Radiative Cooling on Scaling Laws of X-Ray Groups and Clusters. ApJ, 552:L27–L30, May 2001. doi: 10.1086/320261.

D. M. Neumann and M. Arnaud. Self-similarity of clusters of galaxies and the L_X-T relation. A&A, 373:L33–L36, July 2001. doi: 10.1051/0004-6361:20010770.

T. B. O'Hara, J. J. Mohr, and A. J. R. Sanderson. Evolution of the Intracluster Medium Between $0.2 < z < 1.3$ in a Chandra Sample of 70 Galaxy Clusters. *ArXiv e-prints*, October 2007.

F. R. Pearce, P. A. Thomas, H. M. P. Couchman, and A. C. Edge. The effect of radiative cooling on the X-ray properties of galaxy clusters. MNRAS, 317:1029–1040, October 2000. doi: 10.1046/j.1365-8711.2000.03773.x.

Planck Collaboration, N. Aghanim, M. Arnaud, M. Ashdown, J. Aumont, C. Baccigalupi, A. Balbi, A. J. Banday, R. B. Barreiro, M. Bartelmann, J. G. Bartlett, E. Battaner, K. Benabed, A. Benoît, J.-P. Bernard, M. Bersanelli, R. Bhatia, J. J. Bock, A. Bonaldi, J. R. Bond, J. Borrill, F. R. Bouchet, M. L. Brown, M. Bucher, C. Burigana, P. Cabella, J.-F. Cardoso, A. Catalano, L. Cayón, A. Challinor, A. Chamballu, R.-R. Chary, L.-Y. Chiang, C. Chiang, G. Chon, P. R. Christensen, E. Churazov, D. L. Clements, S. Colafrancesco, S. Colombi, F. Couchot, A. Coulais, B. P. Crill, F. Cuttaia, A. da Silva, H. Dahle, L. Danese, P. de Bernardis, G. de Gasperis, A. de Rosa, G. de Zotti, J. Delabrouille, J.-M. Delouis, F.-X. Désert, J. M. Diego, K. Dolag, S. Donzelli, O. Doré, U. Dörl, M. Douspis, X. Dupac, G. Efstathiou, T. A. Enßlin, F. Finelli, I. Flores-Cacho, O. Forni, M. Frailis, E. Franceschi, S. Fromenteau, S. Galeotta, K. Ganga, R. T. Génova-Santos, M. Giard, G. Giardino, Y. Giraud-Héraud, J. González-Nuevo, K. M. Górski, S. Gratton, A. Gregorio, A. Gruppuso, D. Harrison, S. Henrot-Versillé, C. Hernández-Monteagudo, D. Herranz, S. R. Hildebrandt, E. Hivon, M. Hobson, W. A. Holmes, W. Hovest, R. J. Hoyland, K. M. Huffenberger, A. H. Jaffe, W. C. Jones, M. Juvela, E. Keihänen, R. Keskitalo, T. S. Kisner, R. Kneissl, L. Knox, H. Kurki-Suonio, G. Lagache, J.-M. Lamarre, A. Lasenby, R. J. Laureijs, C. R. Lawrence, S. Leach, R. Leonardi, M. Linden-Vørnle, M. López-Caniego, P. M. Lubin, J. F. Macías-Pérez, C. J. MacTavish, B. Maffei, D. Maino, N. Mandolesi, R. Mann, M. Maris, F. Marleau, E. Martínez-González, S. Masi, S. Matarrese, F. Matthai, P. Mazzotta, A. Melchiorri, J.-B. Melin, L. Mendes, A. Mennella, S. Mitra, M.-A. Miville-Deschênes, A. Moneti, L. Montier, G. Morgante, D. Mortlock, D. Munshi, A. Murphy, P. Naselsky, P. Natoli, C. B. Netterfield, H. U. Nørgaard-Nielsen, F. Noviello, D. Novikov, I. Novikov, S. Osborne, F. Pajot, F. Pasian, G. Patanchon, O. Perdereau, L. Perotto, F. Perrotta, F. Piacentini, M. Piat, E. Pierpaoli, R. Piffaretti, S. Plaszczynski, E. Pointecouteau, G. Polenta, N. Ponthieu, T. Poutanen, G. W. Pratt, G. Prézeau, S. Prunet, J.-L. Puget, R. Rebolo, M. Reinecke, C. Renault, S. Ricciardi, T. Riller, I. Ristorcelli, G. Rocha,

C. Rosset, J. A. Rubiño-Martín, B. Rusholme, M. Sandri, D. Santos, B. M. Schaefer, D. Scott, M. D. Seiffert, G. F. Smoot, J.-L. Starck, F. Stivoli, V. Stolyarov, R. Sunyaev, J.-F. Sygnet, J. A. Tauber, L. Terenzi, L. Toffolatti, M. Tomasi, M. Tristram, J. Tuovinen, L. Valenziano, L. Vibert, P. Vielva, F. Villa, N. Vittorio, B. D. Wandelt, S. D. M. White, M. White, D. Yvon, A. Zacchei, and A. Zonca. Planck early results. X. Statistical analysis of Sunyaev-Zeldovich scaling relations for X-ray galaxy clusters. A&A, 536:A10, December 2011. doi: 10.1051/0004-6361/201116457.

G. W. Pratt, J. H. Croston, M. Arnaud, and H. Böhringer. Galaxy cluster X-ray luminosity scaling relations from a representative local sample (REXCESS). A&A, 498:361–378, May 2009. doi: 10.1051/0004-6361/200810994.

W. H. Press and M. Davis. How to identify and weigh virialized clusters of galaxies in a complete redshift catalog. ApJ, 259:449–473, August 1982. doi: 10.1086/160183.

W. H. Press and P. Schechter. Formation of Galaxies and Clusters of Galaxies by Self-Similar Gravitational Condensation. ApJ, 187:425–438, February 1974. doi: 10.1086/152650.

T. H. Reiprich and H. Böhringer. The Mass Function of an X-Ray Flux-limited Sample of Galaxy Clusters. ApJ, 567:716–740, March 2002. doi: 10.1086/338753.

H. Shan, J.-P. Kneib, C. Tao, Z. Fan, M. Jauzac, M. Limousin, R. Massey, J. Rhodes, K. Thanjavur, and H. J. McCracken. Weak Lensing Measurement of Galaxy Clusters in the CFHTLS-Wide Survey. ApJ, 748:56, March 2012. doi: 10.1088/0004-637X/748/1/56.

Z. Shang, B. J. Wills, D. Wills, and M. S. Brotherton. Spectral Properties from Lyα to Hα for an Essentially Complete Sample of Quasars. I. Data. AJ, 134:294–393, July 2007. doi: 10.1086/518505.

C. J. Short, P. A. Thomas, O. E. Young, F. R. Pearce, A. Jenkins, and O. Muanwong. The evolution of galaxy cluster X-ray scaling relations. MNRAS, 408:2213–2233, November 2010. doi: 10.1111/j.1365-2966.2010.17267.x.

C. J. Short, P. A. Thomas, and O. E. Young. Heating and enriching the intracluster medium. MNRAS, 428:1225–1247, January 2013. doi: 10.1093/mnras/sts107.

V. Springel, S. D. M. White, G. Tormen, and G. Kauffmann. Populating a cluster of galaxies - I. Results at [formmu2]z=0. MNRAS, 328:726–750, December 2001. doi: 10.1046/j.1365-8711.2001.04912.x.

V. Springel, S. D. M. White, A. Jenkins, C. S. Frenk, N. Yoshida, L. Gao, J. Navarro, R. Thacker, D. Croton, J. Helly, J. A. Peacock, S. Cole, P. Thomas, H. Couchman, A. Evrard, J. Colberg, and F. Pearce. Simulations of the formation, evolution and clustering of galaxies and quasars. Nature, 435:629–636, June 2005. doi: 10.1038/nature03597.

R. Stanek, D. Rudd, and A. E. Evrard. The effect of gas physics on the halo mass function. MNRAS, 394:L11–L15, March 2009. doi: 10.1111/j.1745-3933.2008.00597.x.

R. Stanek, E. Rasia, A. E. Evrard, F. Pearce, and L. Gazzola. Massive halos in millennium gas simulations: Multivariate scaling relations. *The Astrophysical Journal*, 715(2):1508, 2010. URL `http://stacks.iop.org/0004-637X/715/i=2/a=1508`.

Z. Staniszewski, P. A. R. Ade, K. A. Aird, B. A. Benson, L. E. Bleem, J. E. Carlstrom, C. L. Chang, H.-M. Cho, T. M. Crawford, A. T. Crites, T. de Haan, M. A. Dobbs, N. W. Halverson, G. P. Holder, W. L. Holzapfel, J. D. Hrubes, M. Joy, R. Keisler, T. M. Lanting, A. T. Lee, E. M. Leitch, A. Loehr, M. Lueker, J. J. McMahon, J. Mehl, S. S. Meyer, J. J. Mohr, T. E. Montroy, C.-C. Ngeow, S. Padin, T. Plagge, C. Pryke, C. L. Reichardt, J. E. Ruhl, K. K. Schaffer, L. Shaw, E. Shirokoff, H. G. Spieler, B. Stalder, A. A. Stark, K. Vanderlinde, J. D. Vieira, O. Zahn, and A. Zenteno. Galaxy Clusters Discovered with a Sunyaev-Zel'dovich Effect Survey. ApJ, 701:32–41, August 2009. doi: 10.1088/0004-637X/701/1/32.

M. Sun. Intracluster star formation and galaxy transformation: ESO 137-001 in A3627. In *HST Proposal*, page 11683, July 2008.

R. S. Sutherland and M. A. Dopita. Cooling functions for low-density astrophysical plasmas. ApJS, 88:253–327, September 1993. doi: 10.1086/191823.

J. A. Tyson, R. A. Wenk, and F. Valdes. Detection of systematic gravitational lens galaxy image alignments - Mapping dark matter in galaxy clusters. ApJ, 349: L1–L4, January 1990. doi: 10.1086/185636.

A. Vikhlinin, R. A. Burenin, H. Ebeling, W. R. Forman, A. Hornstrup, C. Jones, A. V. Kravtsov, S. S. Murray, D. Nagai, H. Quintana, and A. Voevodkin. Chandra Cluster Cosmology Project. II. Samples and X-Ray Data Reduction. ApJ, 692: 1033–1059, February 2009. doi: 10.1088/0004-637X/692/2/1033.

G. M. Voit. Tracing cosmic evolution with clusters of galaxies. *Reviews of Modern Physics*, 77:207–258, April 2005. doi: 10.1103/RevModPhys.77.207.

G. M. Voit, S. T. Kay, and G. L. Bryan. The baseline intracluster entropy profile from gravitational structure formation. MNRAS, 364:909–916, December 2005. doi: 10.1111/j.1365-2966.2005.09621.x.

Y. B. Zeldovich and R. A. Sunyaev. The Interaction of Matter and Radiation in a Hot-Model Universe. Ap&SS, 4:301–316, July 1969. doi: 10.1007/BF00661821.

Y.-Y. Zhang, A. Finoguenov, H. Böhringer, J.-P. Kneib, G. P. Smith, R. Kneissl, N. Okabe, and H. Dahle. LoCuSS: comparison of observed X-ray and lensing galaxy cluster scaling relations with simulations. A&A, 482:451–472, May 2008. doi: 10.1051/0004-6361:20079103.

F. Zwicky. Die Rotverschiebung von extragalaktischen Nebeln. *Helvetica Physica Acta*, 6:110–127, 1933.

F. Zwicky. Nebulae as Gravitational Lenses. *Physical Review*, 51:290–290, February 1937. doi: 10.1103/PhysRev.51.290.